Additive Manufacturing 66 (2023) 103476

Contents lists available at ScienceDirect

Additive Manufacturing

journal homepage: www.elsevier.com/locate/addma

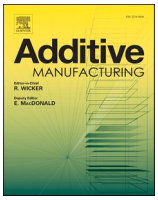

In situ interlayer hot forging arc-based directed energy deposition of Inconel® 625: process development and microstructure effects☆

Francisco Werley Cipriano Farias [a,*], Valdemar R. Duarte [a,b], Igor Oliveira Felice [a], João da Cruz Payão Filho [c], Norbert Schell [d], Emad Maawad [d], J.A. Avila [e], J.Y. Li [f], Y. Zhang [f], T. G. Santos [a,b], J.P. Oliveira [a,g,**]

[a] UNIDEMI, Department of Mechanical and Industrial Engineering, NOVA School of Science and Technology, NOVA University of Lisbon, 2829-516 Caparica, Portugal
[b] Laboratório Associado de Sistemas Inteligentes, LASI, 4800-058 Guimarães, Portugal
[c] Program of Metallurgical and Materials Engineering, Federal University of Rio de Janeiro (UFRJ), CEP 21941-972 Rio de Janeiro, RJ, Brazil
[d] Helmholtz-Zentrum Hereon, Institute of Materials Physics, Max-Planck-Str. 1, Geesthacht 21502, Germany
[e] Department of Strength of Materials and Structural Engineering, Barcelona School of Engineering (ETSEIB), Universitat Politècnica de Catalunya, Barcelona, Spain
[f] Herbert Gleiter Institute of Nanoscience, School of Materials Science and Engineering, Nanjing University of Science and Technology, Nanjing 210094, China
[g] CENIMAT|i3N, Department of Materials Science, School of Science and Technology, NOVA University Lisbon, Caparica, Portugal

ARTICLE INFO

Keywords:
Wire arc additive manufacturing
Inconel
Hybrid process
Hot forging
Heat treatment
Equiaxed grains

ABSTRACT

The typical as-built coarse and cube-oriented microstructure of Inconel® 625 parts fabricated via arc-based directed energy deposition (DED) induces anisotropic mechanical behavior, reducing the potential applications of arc-based DEDed Inconel® 625 in critical components. In this sense, the present work aimed to reduce the grain size and texture by applying an in situ interlayer hot forging (HF) combined with post-deposition heat treatments (PDHT). The produced samples were characterized through optical microscopy, scanning electron microscopy coupled with electron backscatter diffraction, synchrotron X-ray diffraction, and Vickers microhardness. Also, a dedicated deformation tool was designed and optimized via a finite element method model considering the processing conditions and thermal cycle experienced by the material. It is shown that the in situ interlayer deformation induced a thermo-mechanical-affected zone (dynamic recrystallized + remaining deformation, with a height of ≈ 1.2 mm) at the bead top surface, which resulted in thinner aligned grains and lower texture index in relation to as-built DED counterpart. In addition, the effects of solution (1100 °C/ 1 h) and stabilization (980 °C/ 1 h) PDHTs on the Inconel® 625 HF-DEDed parts were also analyzed, which promoted fine and equiaxed static recrystallized grains without cube orientation, comparable to wrought material. Therefore, the HF-DED process significantly refined the typical coarse and highly oriented microstructure of Ni-based superalloys obtained by arc-based DED.

1. Introduction

Directed energy deposition (DED[1]) additive manufacturing processes, especially arc-based ones (also known as wire arc additive manufacturing – WAAM®), have high deposition rates (2 – 6 kg/h), which makes them appropriate to fabricate medium to high volume metal parts as well as for being used in repair operations [1]. Arc-based DED systems consist of a heat source (a commercial welding machine, e.g., gas metal arc – GMA) that melts the feedstock material (in the form of wire) and a movement system (e.g., a robotic arm or CNC machine) that follows a previously optimized deposition strategy [2,3]. Arc-based DED produces a primary part close to the final desired geometry, reducing the material waste and post-processing time and cost (e.g., by machining methods) [4–6]. Arc-based DED processes are especially advantageous

☆ One of the authors of this article is part of the Editorial Board of the journal. To avoid potential conflicts of interest, the responsibility for the editorial and peer-review process of this article lies with the journal's other editors. Furthermore, the authors of this article were removed from the peer review process and had no, and will not have any access to confidential information related to the editorial process of this article.

* Corresponding author.
** Corresponding author at: CENIMAT|i3N, Department of Materials Science, School of Science and Technology, NOVA University Lisbon, Caparica, Portugal.
E-mail addresses: fw.farias@campus.fct.unl.pt (F.W.C. Farias), jp.oliveira@fct.unl.pt (J.P. Oliveira).

[1] The terminology adopted in the present work followed the ASTM F3187 – 16 and ISO/ASTM 52900 – 2021.

https://doi.org/10.1016/j.addma.2023.103476
Received 14 November 2022; Received in revised form 3 February 2023; Accepted 1 March 2023
Available online 3 March 2023

for high-cost alloys and low-machinability materials (e.g., Ti- and Ni-based alloys). In this context, Moor et al. [7] and English et al. [8] assessed that arc-based DED could promote savings of up to 25–30 % in the fabrication of Ni-based superalloys parts with complex geometries (e.g., fittings, impellers, and spars for the aeronautic industry) [9] when compared to traditional manufacturing routes (e.g., machining from a billet) due to minimization of the buy-to-fly ratio and machining time [10,11]. Additionally, due to the absence of dies and other dedicated tools, arc-based DED increases the production chain flexibility and promotes decentralization, which is especially advantageous for unconventional spare parts manufacturing (shorter lead times) [12].

Despite the abovementioned advantages, Ni-based superalloys parts fabricated via arc-based DED, especially Inconel® 625 and Inconel® 718, have critical material- and process-related challenges [13,14]. Among them, it can highlight the coarse columnar grains and a highly oriented microstructure [15–17], high distortions and residual stress levels [18], low printability (susceptible to hot cracks) [19], poor heat treatment response [20–23], and inferior mechanical properties (i.e., does not meet the ASTM B 446 – 03) and corrosion resistance (both electrolytic and oxidation) [24–28], which can limit the full industrial adoption of arc-based DED in the oil & gas, aeronautics, nuclear, and naval fields for critical engineering parts owing to rigid standards requirements (e.g., API 6ACRA, DNVGL-ST-F101, and AMS 5662 standards).

In this scenery, arc-based DED variants, hybrid processes, and redesign of the feedstock material composition have been developed to induce grain size refinement (columnar to equiaxial transition [29] or recrystallization [30]) and reduce solidification segregation [31], which can be achieved by the use of ultrasound vibrations [32–34], external magnetic field [35], interlayer (cold or hot) deformation [36–38], forced cooling systems [39], the addition of inoculants in the melt pool [40], and increase the feedstock material alloying elements content [41]. Among these alternatives, the interlayer mechanical deformation variants stand out for simultaneously reducing the residual stress (promoting local yielding), inducing grain size refinement (via dynamic and static recrystallization mechanisms), and not altering the feedstock material specification [42]. Deposition + interlayer deformation (rolling, peening, or forging) was first employed in arc-based welding to improve the welded joint fatigue life (relieving residual stresses) and filler metal weldability [43–46]. However, considering the typical geometric aspects associated with additive manufacturing (complex 3D geometries and no deformation restrictions), the DED + interlayer deformation has challenges related to higher residual stresses, non-linear path planning, and coupled deposition and deformation parameters (i.e., avoiding the entire remelt of the deformed zone and not induce deposition defects due to layer morphology modification). In addition, typical commercials alloys fabricated by arc-based DED (e.g., Ti-6Al-4 V [47], Al series 2xxx [48], AISI 316 L stainless steel [49], and Inconel® 718 [50]) showed adequate formability, reinforcing the potential use of arc-based DED + interlayer deformation.

Concerning Ni-based superalloys, to the best of the authors' knowledge, only Zhao et al. [51] (laser-DED + interlayer hot rolling) and Li et al. [52] (laser-DED + interlayer hot micro-forging) studied the solid-solution strengthened superalloys (Ni 60 and Ni80-Cr20 alloys, respectively) fabricated by DED + interlayer deformation. These authors [51,52] observed that the interlayer deformation induced a finer and less oriented microstructure, increased the microhardness, and reduced the wear rate in relation to the deformation-free DED counterparts. For precipitation-strengthened superalloys, only Inconel® 718 was studied. Xu et al. [53] and Hönnige et al. [18] (GMA-DED + interlayer cold rolling), Zhang et al. [54] and Chen et al. [55] (GMA-DED + interlayer hot rolling), Li et al. [36] (laser-DED + interlayer hot rolling), and Wang et al. [56] (laser-DED + interlayer cold peening) observed that the interlayer deformation induced a grain size similar to that of wrought material (e.g., 8 [36], 12.7 [53], 25 ~ 30 μm [54], and vs. 15 μm; both after the homogenization heat treatment) and a low crystallographic texture index (< 3), improved the post-deposition heat treatment response, and enhanced the quasi-static mechanical properties (meeting the AMS 5662 requirements). Despite the efficient grain size refinement and residual stress relieving due to interlayer cold or hot rolling, the low path planning flexibility may limit its industrial scalability [57]. In addition, both rolling, forging, and peening required a dedicated auxiliary facility with high structural rigidity to enable material deformation.

Recently, to overcome the path planning limitations and deposition strategies restrictions, Duarte et al. [58] developed a GMA-DED process coupled with an in situ coaxial hot forging mechanism, which deformed the newly consolidated feedstock material and allowed unrestricted changes in planar deposition directions. Furthermore, Duarte et al. [58] reported that the in situ interlayer hot forging reduced the residual stress and refined the microstructure of a CuAl8 alloy fabricated by GMA-DED. Thus, considering the commonly observed coarse and highly oriented microstructure of the Inconel® 625 fabricated by GMA-DED (both in as-built and post-deposition heat-treated conditions) [13–28], the present work aimed to refine the grain size and reduce the texture of the Inconel® 625 fabricated by GMA-DED via an in situ interlayer coaxial hot forging variant. To optimize the forging temperature, the coaxial hammer was designed based on the thermal profile obtained through a thermo-metallurgical finite element method (FEM) model. Inconel® 625 GMA-DEDed parts (with and without in situ interlayer hot forging) were microstructurally characterized through optical microscopy (OM), scanning electron microscopy (SEM) coupled with electron backscatter diffraction (EBSD), synchrotron X-ray diffraction (SXRD) and microhardness. Finally, the effect of post-deposition heat treatments (solution and stabilization annealing) on Inconel® 625 fabricated by GMA-DED + in situ interlayer hot forging was also evaluated.

2. Materials and methods

2.1. Materials and process description

An AWS A5.14 ERNiCrMo-3 (UNS N06625; Inconel® 625) filler metal wire (diameter of 1.2 mm) was deposited on an ASTM A36 Q235 hot rolled carbon steel plate (80 × 10 ×200 mm^3) to build single-bead 10-layer walls. The arc-based DED machine consisted of a KEMPY PRO MIG 3200 power source (gas metal arc – GMA) coupled to an in-house developed 3-axis CNC machine [59]. Table 1 summarizes the main deposition parameters, which were previously optimized considering the feedstock material supplier (ESAB®) guidelines. The electric current and arc plasma voltage oscillograms were acquired with a data acquisition system and a LEM LA 200-P current probe (sampling rate of

Table 1
Arc plasma-DED + in situ interlayer hot forging parameters.

Arc plasma-DED		
Electric current[a]	72.1	[A]
Arc plasma voltage[a]	17.1	[V]
Wire feed speed	3.5	[m/min]
Travel speed	5.0	[mm/s]
Heat input[b]	209.6	[J/mm]
Idle time	90	[s]
Wire diameter	1.2	[mm]
Contact tip to work distance	10	[mm]
Shielding gas	Ar (Type II; Grade C)	
Shielding gas specification	AWS A5.32	
Shielding gas flow	15	[l/min]
Linear deposition length	100	[mm]
Layer numbers	10	
Substrate preparation	ISO 8501–1	
In situ interlayer hot forging		
Pneumatic pressure	5	[MPa]
Frequency	8	[Hz]

[a] Root mean square
[b] Thermal efficiency (η = 0.85) [60]

5 kHz).

2.1.1. In situ interlayer hot forging system

The in situ interlayer hot forging system, detailed in Fig. 1, consists of two pneumatics actuators (Festo ADN-12–10-I-P-A) positioned symmetrically in relation to the welding torch that pushes/pulls the moving parts (gas nozzle and the circular crown hammer, which are mounted on a linear bearing), which hot deformed the material immediately after the deposition. The main in situ interlayer hot forging parameters are the forging force (operationally expressed by the pneumatic pressure) and the forging temperature (operationally expressed by the circular crown hammer radius). The smaller the hammer radius, the higher the forging temperature. For more details on the in situ interlayer hot forging design, parameters, and equipment, see Duarte et al. [58].

2.1.2. Post-deposition heat treatments

Post-deposition heat treatments (PDHT) were performed in a furnace with a heating rate of 20 °C/s. The soaking time was 1 h at the peak temperature, and the cooling rate was 20 °C/s. The PDHTs (solution and stabilization annealing) followed the Inconel® 625 specification (ASTM B 446). The solution annealing (1100 °C/1 h) is used to promote the Laves phase dissolution [20,60] and the homogenization of the solidification (as-built) interdendritic segregation. The stabilization annealing (980 °C/1 h) promotes the MC-type carbide precipitation (stabilization), preventing M_6C-type carbide precipitation and alloy sensitization [61,62]. In addition, the literature [20–22,53,63,64] highlighted that the PDHT had a negligible effect on the grain size, grain morphology, and crystallographic texture of Ni-based superalloys fabricated by GMA-DED, which was related to the low driving force (dislocation density and in-process developed deformation) for recrystallization or significant grain boundary mobility. Thus, GMA-DEDed Ni-based superalloys retain the primary solidification grain microstructure even after PDHT. In opposition, high-density energy DED processes (e.g., laser-based) can undergo static recrystallization during the solution annealing due to the higher residual deformation developed during the deposition [60,65,66]. Thus, since it is consensus that PDHT does not promote significant grain size and grain morphology changes in Ni-based superalloys obtained by GMA-DED and considering the present objective (refining the grain size and reducing the texture), the stabilization and solution annealing PDHTs were carried out only in the arc-based DED + in situ interlayer hot forging (HF-DED) specimens.

2.1.3. Hot forging dynamic characterization

The hot forging system was dynamically characterized to assess the forging conditions by measuring the hammer speed and deceleration, which were used to calculate the forging force and strain rate during the in situ interlayer hot forging. A Photron FASTCAM Mini WX50 high-speed camera (operating at 10,000 fps and 512 × 256 pixels) with a Nikon AF NIKKOR 28–105 mm macro lens was used. Data post-processing was performed using a Python-based routine, where the frames were binarized, allowing acquired the instantaneous position of the moving parts (see Section 2.1.1).

A Fluke TI400 infrared camera (7.5–14 μm wavelength) with an acquisition rate of 9 Hz and a resolution of 320 × 240 pixels was used to measure the forging temperature. To select the emissivity (0.76), the infrared camera thermal cycle was previously validated with thermocouples.

2.2. Microstructural characterization

The microstructure of the Inconel® 625 fabricated by GMA-DED was characterized via OM (Leica DMI 5000 M) and SEM (SU3800 Hitachi). The metallographic specimens were, in sequence, ground, polished, and electrolytically etched (10 wt. % chromium trioxides – Cr_2O_3 – in water,

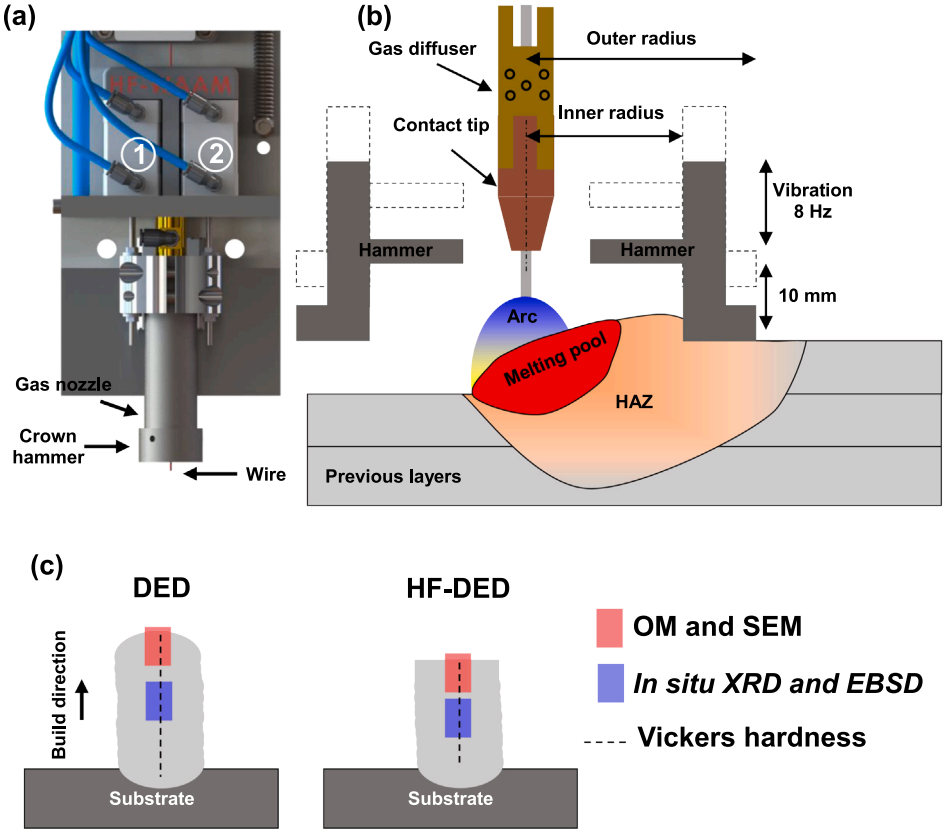

Fig. 1. Schematic representation of the arc-based DED + in situ interlayer hot forging: equipment (a) and process (b), and (c) location where the microstructure characterization was performed at printed walls. HAZ corresponds to the heat-affected zone; ① and ② are the pneumatic actuators.

5 V for 20 s). Fig. 1c shows the position in the samples where the metallographic analyses were performed. The EBSD specimens followed a metallographic procedure to that used for OM and SEM adding a final mechanical polishing step with colloidal silica, 0.04 μm, for 2 h. EBSD data post-processing was carried out using the open-source MTEX® Toolbox [67]. Misorientations higher than 15° were considered high-angle grain boundaries. The grain size was measured through the intercept method (ASTM E 112) using a square grid [68].

2.2.1. Vickers microhardness

Vickers microhardness (Mitutoyo HM-112) profiles (straight vertical line through the entire wall; Fig. 1b) were performed using a load of 0.3 kgf ($HV_{0.3}$), a dwell time of 15 s, and an indentation distance of 0.5 mm, following the ISO 6507–1 standard.

2.2.2. Synchrotron X-ray diffraction

Synchrotron X-ray diffractions (SXRD) were conducted at the High Energy Materials Science P07 beamline of PETRA III at the DESY synchrotron. A wavelength of 0.14235 Å (87.09 keV) was used. Rectangle samples (10 × 20 mm^2; Fig. 1c) with a thickness of 2 mm were used, and the X-ray beam was focused on the middle of the samples. Before X-ray exposure, the samples were ground and polished. A 2D Perkin Elmer detector with a pixel size of 200 × 200 μm^2 was used to acquire the Debye-Scherrer diffraction rings, which were integrated along the full azimuthal angle to acquire the typical 2θ × intensity diffraction patterns. SXRD beam spot size and exposure time were 1 × 1 mm^2 and 4 s, respectively. The instrumental peak broadening was determined using LaB_6 (calibrant powder). For more details about SXRD set-up and data post-processing, see Rodrigues et al. [69].

2.3. GMA-DED modeling

To assess the thermal profile during deposition and estimate the ideal hot forging stroke position, a thermo-metallurgical finite element method (FEM) model was developed based on an Inconel® 625 10-layer single-bead wall deposited by GMA-DED. This model was developed using the commercial ESI Sysweld® FEM software. The actual physical dimensions of the substrate and GMA-DEDed wall and measured deposition parameters were used as model inputs. Fig. 2 depicts the model configuration and mesh size. In addition, two k-type thermocouples, positioned at 9 and 14 mm (red dots in Fig. 2) from the deposited bead edge, were used to validate the simulation results experimentally.

The present model was based on the energy balance and the multi-phase transient heat flux with a volumetric and mobile heat source (modified Fourier equation; Eq. 1) [70,71]. T, v, k, ρ, c_p, and $\dot{Q}$ are the temperature, deposition velocity, thermal conductivity, density, specific heat, and the volumetric heat source, respectively. Both the feedstock material and substrate isotropic physical properties (k, ρ, and c_p) were extracted from the ESI Sysweld® material database (detailed in the Supplementary material). $\dot{Q}$ was modeled using the Goldak's double-ellipsoidal [72]. The heat source geometrical and deposition electric parameters (refer to Table 1) are available in the Supplementary material. The initial ($t = 0$; Eq. 2) and boundary (Eq. 3) conditions considered that all the activated mesh nodes were at 27°C (T_0) and the radiation and convection flux occurred on the model surface, respectively. $\vec{n}$, ε, σ, and h are a unitary vector perpendicular to the model surface, the Stefan–Boltzmann constant, the gray body emissivity (0.76), and the convective heat transfer coefficient, respectively. h was defined as 20 $W{\bullet}m^{-2}{\bullet}K^{-1}$ for the surfaces exposed to air and 100 $W{\bullet}m^{-2}{\bullet}K^{-1}$ for the substrate bottom surface (simulating the heat flux to the welding table) [73].

$$\frac{\partial}{\partial x}\left(k\frac{\partial T}{\partial x}\right)+\frac{\partial}{\partial y}\left(k\frac{\partial T}{\partial y}\right)+\frac{\partial}{\partial z}\left(k\frac{\partial T}{\partial z}\right)+\dot{Q}=\rho c_p\left(\frac{\partial T}{\partial t}-v\frac{\partial T}{\partial x}\right) \quad (1)$$

$$T(x,y,z,t=0)=T_0=27^{\circ}C \quad (2)$$

$$-\left\langle\frac{\partial T}{\partial x},\frac{\partial T}{\partial y},\frac{\partial T}{\partial z}\right\rangle\cdot\vec{n}=\varepsilon\sigma\left(T^4-T_0^4\right)+h(T-T_0) \quad (3)$$

It is worth noting that multi-layered single-bead DED models are symmetric in relation to the plane formed by the deposition and built directions. Thus, a Neuman boundary condition along the heat source path was adopted to reduce the computational time. Also, although the GMA-DEDed layers are arc-shaped, rectangular-shaped beads reduce the simulation error and computational time and simplify the meshing process [74,75]. The model mesh had 12,800 3D hexahedral elements and 16,609 nodes. The layers were finely meshed (2 × 1.5 × 0.46 mm^3, as shown in Fig. 2) to precisely predict the temperature during the deposition, even considering the intense thermal gradient associated with the GMA-DED. The layers elements were simulated using the birth-and-death technique [76], and the substrate elements were progressively coarsened from the bead edge. Furthermore, the GMA-DED model simulation performance, documentation, and validation followed the ISO 18166 standard recommendations.

3. Results and discussion

3.1. Crown hammer design

3.1.1. GMA-DED modeling validation

Fig. 3 compares the simulated thermal cycles with the temperature evolution measured by thermocouples. Proper matching in both heating and cooling thermal cycles was observed. Measured and simulated peak temperatures in all layers are similar, with maximum relative errors of 11.6 % and 8.0 % (thermocouple at 14 mm, 1st and 2nd layers, respectively). For other layers, the maximum relative error is around 5 %. The small difference between the simulated and measured results can be attributed to three main sources: i) the not exact idle time (90 s)

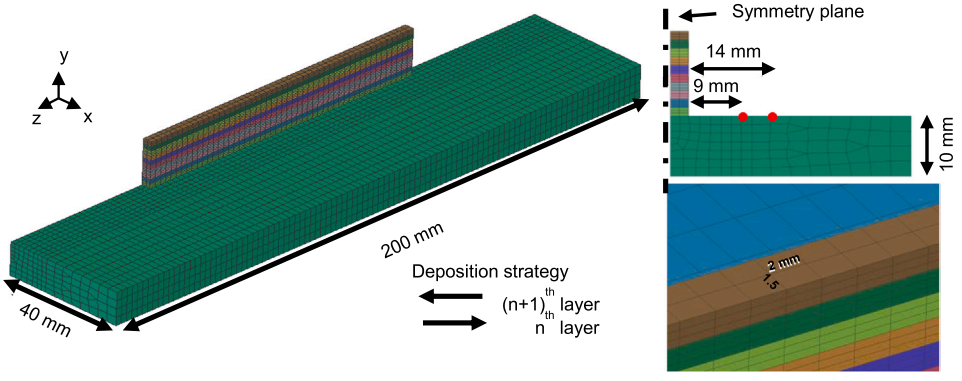

Fig. 2. Finite element model mesh. The red dots represent the position of thermocouples.

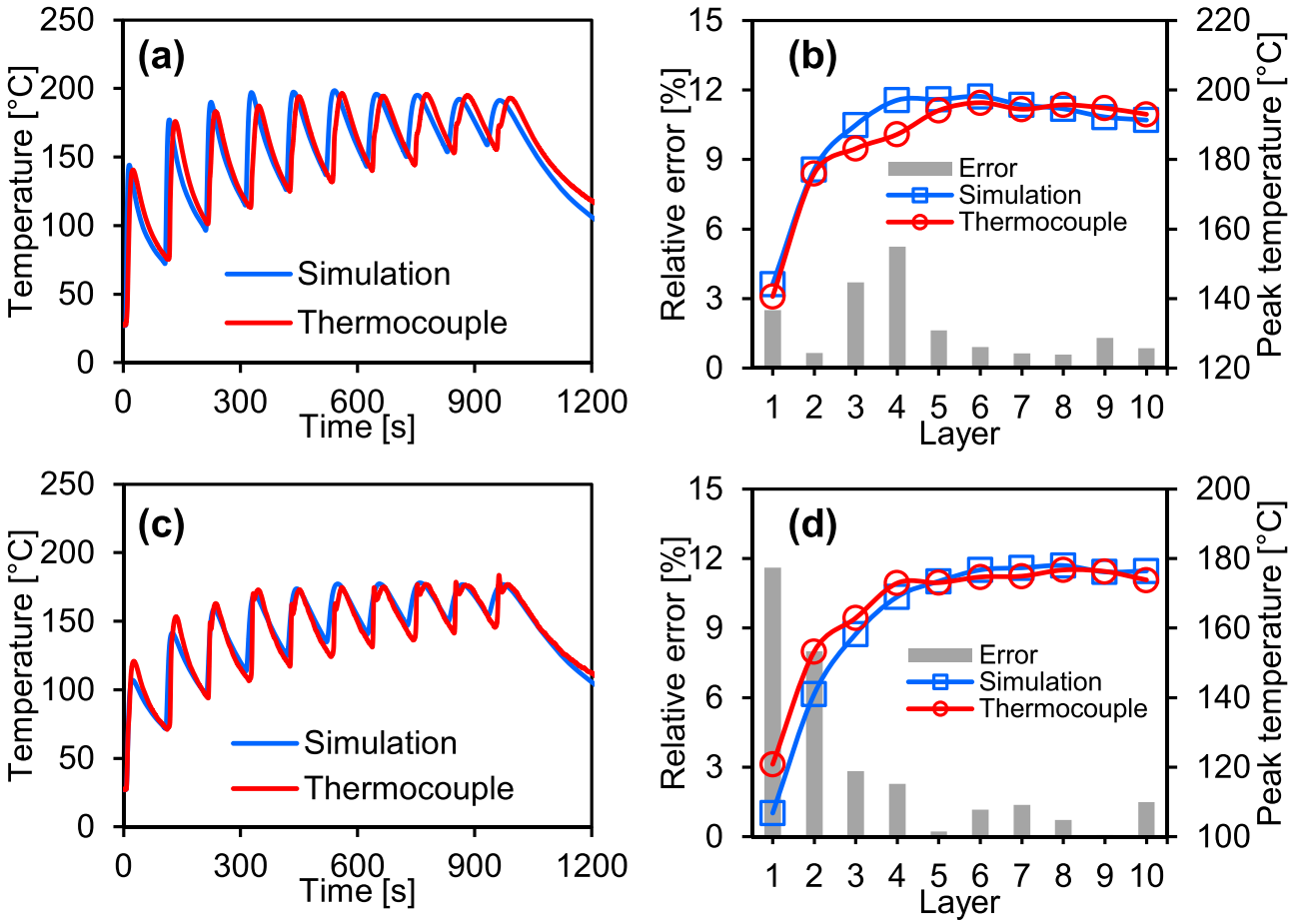

Fig. 3. Thermocouple and FEM model thermal cycles obtained at a point located 9 (a-b) and 14 mm (c-d) from the bead edge.

between layers, which can induce some difference in the observed peak temperature and a non-temporal matching; ii) intrinsic variations (~ 1 – 2 mm) of the contact to work distance during deposition, which can increase the arc power (maintained constant in the FEM model) [77]; iii) slight difference in physical properties (k, ρ, and c_p) of the feedstock and substrate materials compared to those obtained from the ESI Sysweld® database [78]. Also, Farias et al. [73] highlighted that discrepancies between the mesh node and the exact thermocouple positions could also be associated with minor peak temperature differences. Despite the differences between measured and simulated thermal cycles, the present model proved to be suitable for accurately estimating the thermal profiles during GMA-DED deposition.

3.1.2. *Forging hammer design*

The validated thermo-metallurgical FEM model (Fig. 2 and Fig. 3) was used to estimate the thermal profile during the deposition (Fig. 4a). Also, according to the Scheil-Gulliver solidification model (Fig. 4b; Thermo-Calc® software), the Inconel® 625 solidification range is from 1340 °C to 1135 °C, which was corroborated by previous experimental data [79–81]. The sum of the melt pool (> 1340 °C) and mushy zone (1135–1340 °C) lengths defines the minimum distance (hammer radius) between the heat source (arc plasma) and the deformation tool. For a smaller hammer radius, the deformation tool will strike over the melt pool, resulting in liquid metal spattering and a poor layer surface [82]. Also, in the mushy zone, the material possesses a liquid film along the grain boundaries (brittle temperature range) and can fracture during localized deformation [83]. Thus, by combining the thermo-metallurgical FEM model and the Scheil-Gulliver solidification data, the minimum hammer radius can be defined (19.3 mm). In addition, the forging zone (5.9 mm, as detailed in Fig. 4) was defined considering the typical Inconel® 625 forging temperatures (900 – 1100 °C) [50,84,85]. Therefore, to ensure that the in situ interlayer hot forging occurs within the usual Inconel® 625 forging temperature range, the inner diameter was set to 20 mm.

Another important aspect of the hammer design is the outer diameter (Fig. 1). Considering the hammer oscillation frequency and the torch travel speed (detailed in Table 1), the hammer forges only 0.625 mm (forging step, Fs) in each stroke [58], which means that the remaining surface of the hammer (up to the outer diameter) will act over the already forged material. Thus, the remaining hammer's surface will serve as a stopper since the hammer will stroke on the previously deformed material. Therefore, the outer diameter of the hammer was set at 25 mm to ensure that the deformation is limited by the previously deformed material, forming an upper flat layer surface. Otherwise, if the hammer's outer radius were equal to the inner radius plus the forging step, slight variations in the deposition conditions would change the minimum forging temperature, resulting in an uneven bead surface. Therefore, from the simulation results, the inner (20 mm) and outer (25 mm) hammer radii were designed, as detailed in Fig. 1. In addition, the thermography (Fig. 4c) showed that the minimum forging temperature (905 °C) matched with the one estimated by the FEM model (900 °C), reinforcing its accuracy. It is worth mentioning that smaller (17.5 mm; - 2.5 mm) and higher (22.5 mm; + 2.5 mm) inner radius hammers were also tested, and the results obtained corroborated the simulation approach methodology for the hammer design, i.e., 17.5 mm stroked the liquid metal and 22.5 mm induces a low deformation at layer surface.

The forging force was calculated using the principle of impulse and momentum via high-speed camera filming. The forging force depends on the hammer speed before contact (1 m/s) and impact time (2.7 μm)

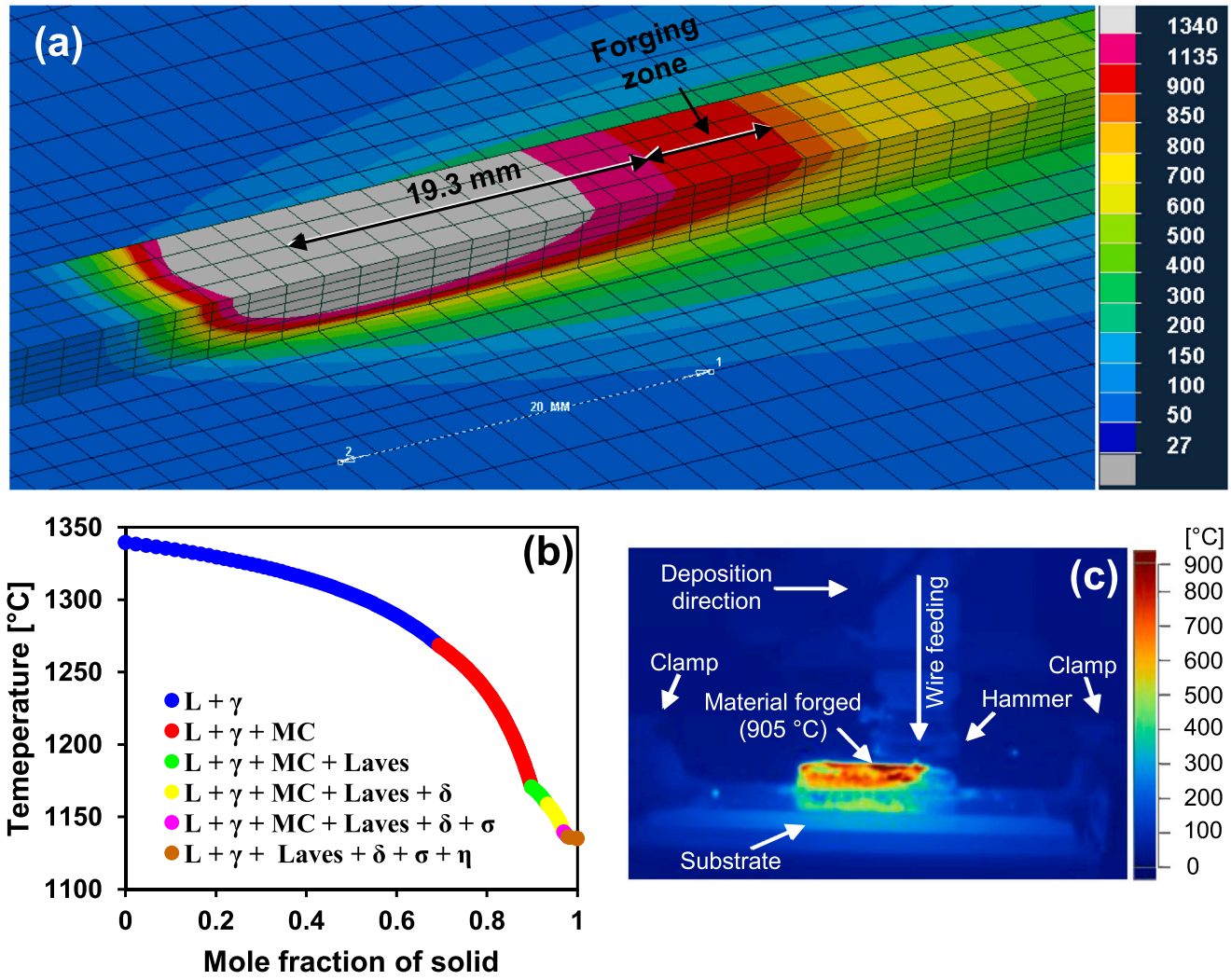

Fig. 4. (a) Simulated thermal profile showing the minimum hammer radius (19.3 mm) and forging zone, (b) Inconel® 625 solidification sequence obtained via Scheil-Gulliver model (Thermo-calc®), and (c) thermal profile obtained via thermography during Inconel® 625 HF-DEDed.

[58]. Therefore, the average measured impact force (1917 N) applied over the forging area (4.18 mm^2) corresponds to an applied stress of 458.6 MPa. Additionally, considering the impact time and true strain (0.11), the average strain rate was estimated (322.2 s^{-1}). Thus, combining the dynamic hammer characterization with the Inconel® 625 flow stress curves (Fig. 5; JMatPro® software), it is possible to identify the forging conditions and the influence of the forging parameters on the amount of strain promoted.

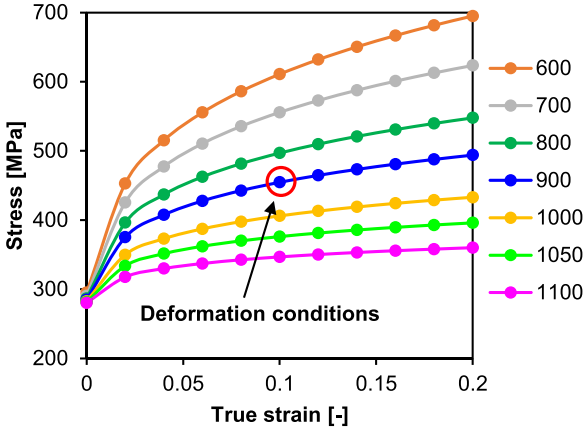

Fig. 5. Inconel® 625 flow stress curves (320 s^{-1}).

In summary, it is possible to conclude that the HF-DED forging temperature and the deformation of the deposited layer can be adjusted by controlling the hammer design, keeping the deposition parameters constant. The inner radius of the hammer will determine the forging temperature, and the outer radius will ensure the deformation uniformity (stress and strain) and a flat final layer surface aspect.

3.2. *In situ effect of interlayer hot forging on the microstructure*

The last layer of the Inconel® 625 fabricated via arc-based DED had the typical Ni-based superalloy as-built microstructure (Fig. 6a), which was in good agreement with the previously observed in the literature [13–28], i.e., this layer was composed by coarse and aligned columnar grains almost parallel to build direction due to the nearly unidirectional heat flux. In addition, the upper region (close to the layer surface) possesses equiaxed dendrites due to the occurrence of the columnar to equiaxed transition (CET), which were induced by the reduction of thermal gradient in the melt pool [16], as described by the Kurz–Giovanola–Trivedi model [86]. However, the length of the CET region is smaller than the subsequent layer deposition penetration (~ 1.34 mm), being observed only in the last deposited layer. The HF-DED samples (Fig. 6b) showed a larger equiaxed zone in relation to DED (1.2

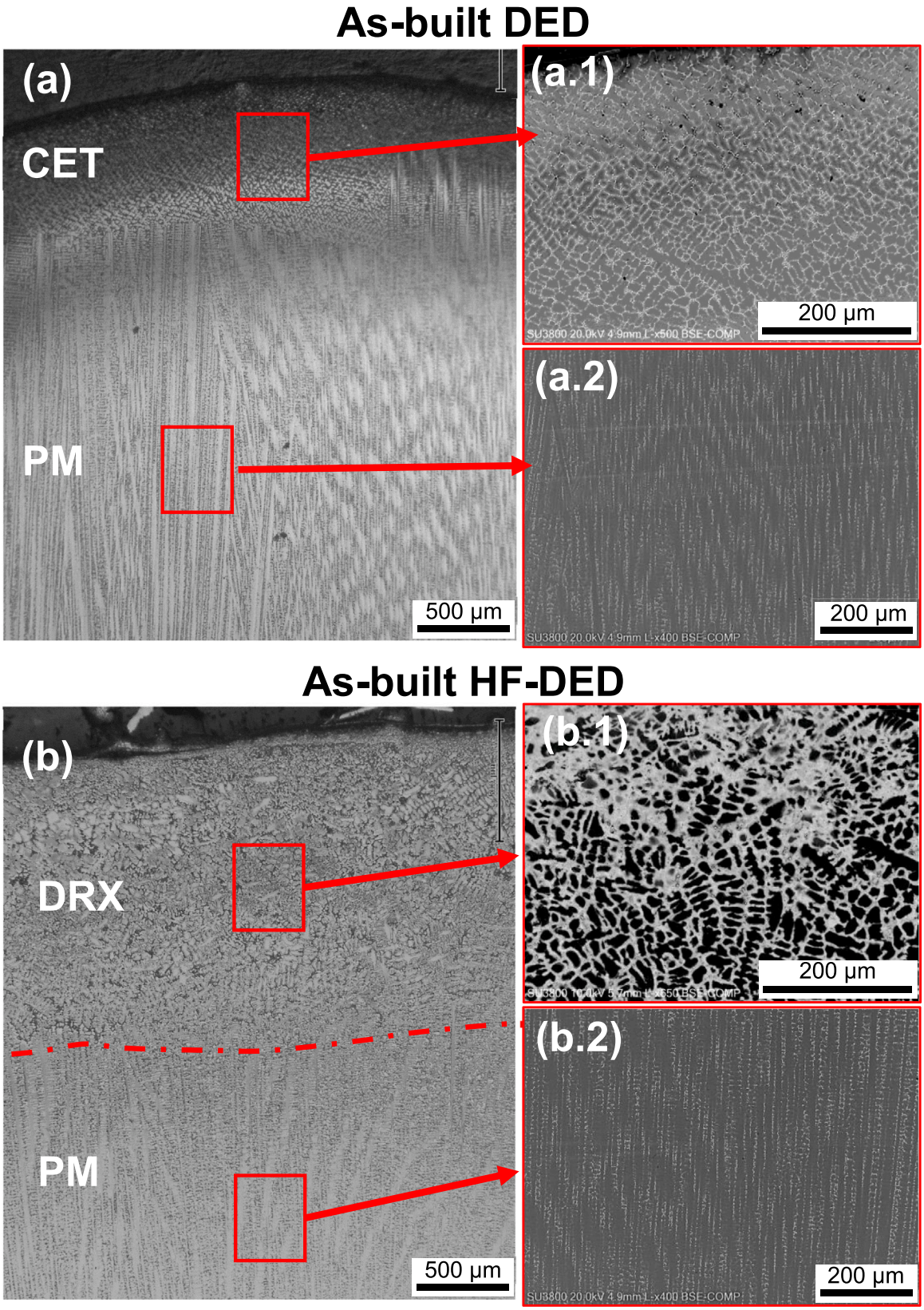

Fig. 6. Last layer (10th) upper surface microstructure: (a) DED and (b) HF-DED. The sub-figures (a.1, a.2, b.1, and b.2) correspond to red rectangles indicated in (a) and (b). CET, PM and DRX mean to columnar to equiaxed transition, primary microstructure, and dynamic recrystallized, respectively.

vs. 0.2 mm), which derivates from the dynamic recrystallization induced by the in situ interlayer hot forging, i.e., the equiaxed grain zone had different origins for the HF-DED (hot deformation) and DED (natural changes in thermal conditions). In addition, the interlayer hot deformation is not enough to completely change the layer microstructure (bead height, ~ 2.5 mm, higher than the dynamically recrystallized zone – 1.2 mm) so that the last deposited layer had two distinct zones: thermo-mechanical-unaffected zone (primary microstructure without remain deformation, PM) and thermo-mechanical-affected zone (dynamic recrystallized grains and deformed primary microstructure).

Fig. 7 compares the interlayer regions between DED and HF-DED conditions. Apart from the top of each sample (Fig. 6), it was observed that the HF-DED promoted overall finer non-aligned dendrites close to the fusion line. However, due to the competitive grain growth in the melt pool, the microstructure turns to be oriented away from the fusion line, similar to that observed by Farias et al. [87] (Inconel® 625 claddings deposited by powder plasma transferred arc welding) and Li et al. [16] (Inconel® 625 parts fabricated by GMA-DED). These results suggest that the HF-DED improves the nucleation sites density at the fusion line, i.e., some remaining dynamic recrystallized grains (non-remelted) or those static recrystallized (reheating thermal cycle) in the thermo-mechanical-affected zone act as epitaxial growth sites, interrupting the coarse and highly oriented grains throughout several layers (as typically observed for the Ni-based superalloys fabricated by arc-based DED processes) and promoting finer and less aligned dendrites from the fusion line [56,88].

The image orientation map (EBSD data detailed in Fig. 8) corroborated the OM and SEM results (Figs. 6 and 7), showing that the DED fusion line had continuous columnar epitaxial grains. In contrast, the HF-DED material showed small equiaxed grains and a thinner and less oriented microstructure compared to its DED counterpart. This latter feature was attributed to the higher number of nucleation sites observed at the fusion line (Figs. 7a and 8b). In addition, the static recrystallization driving force and kinetics depend on the deformation level, peak temperature, and time [89]. Also, considering the high penetration of arc plasma-DED processes and fast cooling rate, the remaining deformation zone had low static recrystallization driving force and kinetics despite undergoing a high peak temperature (just below the melting temperature), which did not induce an intensity static recrystallization close to fusion line for HF-DED during the reheating thermal cycles (Fig. 8d andFigure 8e), as typically visualized in the heat-affected zone of cold rolled plates welded [90] or interlayer cold deformed DEDed parts [18].

The meso-texture was evaluated using the EBSD data and expressed by the orientation distribution function (ODF; Fig. 8c and f) and pole figures (PF; Fig. 9), which showed that the HF-DED had a less oriented microstructure (5.4 vs. 7.6 index). However, both conditions had the typical fusion-based processes crystallographic texture (cube component, (<100>{100}) [53]. In addition, the HF-DED material also showed some rotation concerning the ideal cube component ($\varphi_1 = 45°$; HF-DED, $\varphi_1 = 45° \pm \sim 15°$), which can be related to the change of top layer surface morphology (from the arc-shape – DED – to flat surface – HF-DED), inducing a deeper penetration at the melt pool center (similar to the first layer deposited at the substrate, i.e., flat surface), which tilted the grains and promoted some rotated cube aspects, as also previously reported by Gustafsson at al. [91] (Inconel® 625 GTA welded) and Eghlimi et al. [92] (duplex stainless steel GTA welded).

The HF-DED lower texture index was related to the recrystallized and equiaxed grains formed in the fusion line and the thinner aligned grains. Therefore, considering the overall maintenance of columnar grains and cube texture aspect, it is possible to indicate that the HF-DED slightly influences the solidification conditions. In addition, the kernel average misorientation (KAM; Fig. 8b, e, and g), which is directly correlated with the geometrically necessary dislocations density [93], depicts that the next layer deposition did not entirely annihilate the HF-DED effects, showing a remaining thermo-mechanical-affected zone that can induce static recrystallization during the subsequent thermal cycles and/or post-deposition heat treatment. From KAM results, it is possible to confirm that the equiaxed grains close to the fusion line were recrystallized (KAM values below 1.5) [94]. Thus, the HF-DED induced thinner

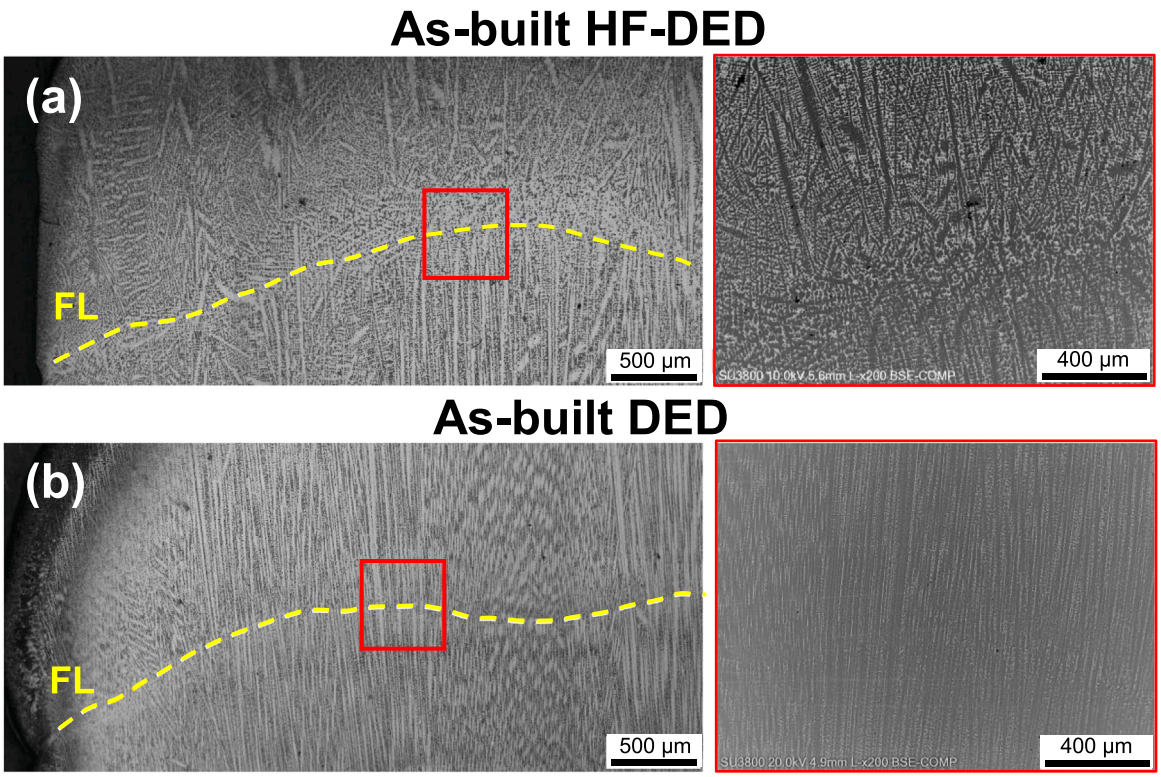

Fig. 7. Comparison of interlayer microstructure on Inconel® 625: (a) HF-DED and (b) DED. FL means fusion line.

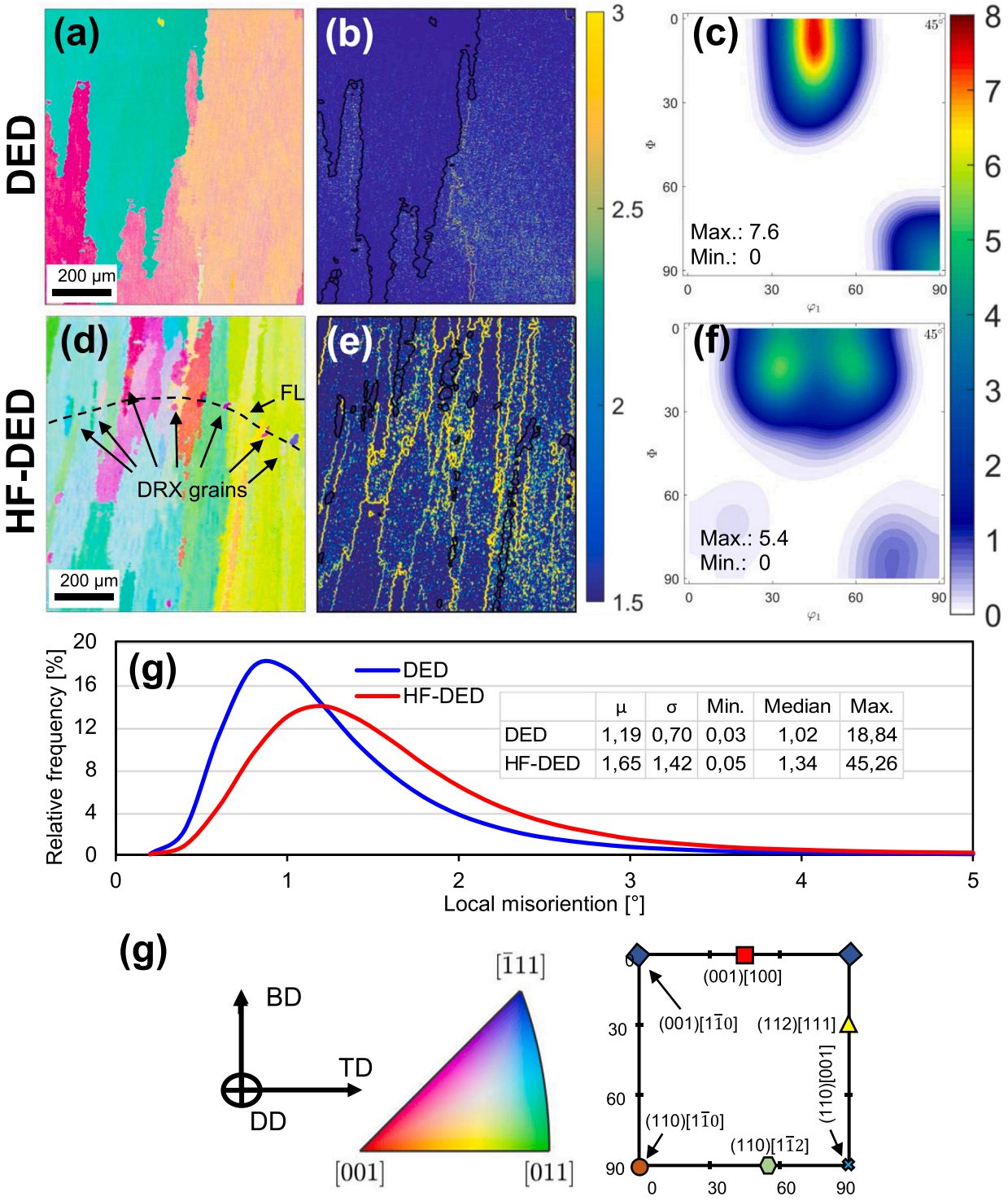

Fig. 8. EBSD analysis of Inconel® 625 DEDed (a-c) and HF-DEDed (d-f). (a) DEDed orientation image map (OIM), (b) kernel average misorientation (KAM) map, and (c) orientation distribution function (ODF; $\varphi_2 = 45°$); (d) HF-DEDed OIM, (e) KAM map, and (f) ODF; (g) KAM distribution; and (h) sample orientation, inverse pole figure color key, and ideal ODF texture components ($\varphi_2 = 45°$). In (g), BD, TD, and DD are the built, transverse, and deposition directions, respectively. In (h), μ and σ represent the average and standard error, respectively.

columnar grains, reduced the texture index, and promoted a remaining thermo-mechanical-affected zone.

The synchrotron X-ray diffraction, 2D Debye-Scherrer rings (Fig. 10), were used to evaluate the meso/macro texture. It can be observed that the DED material did not possess any continuous rings but rather had spotty features, which is a clear indication of coarse grains and highly oriented microstructure. *In situ* interlayer HF induced the formation of almost continuous diffraction rings and reduced the "spotty feature", indicating a finer and less oriented microstructure. The 2D Debye-Scherrer rings analysis supports the EBSD data (ODFs and PFs), i.e., the HF-DED has a less oriented and more refined microstructure. In addition, the synchrotron X-ray diffraction 2D Debye-Scherrer rings were fully integrated along the azimuthal angle (−180 to 180°) to evaluate the diffraction pattern (2θ vs. intensity) as shown in Fig. 11,

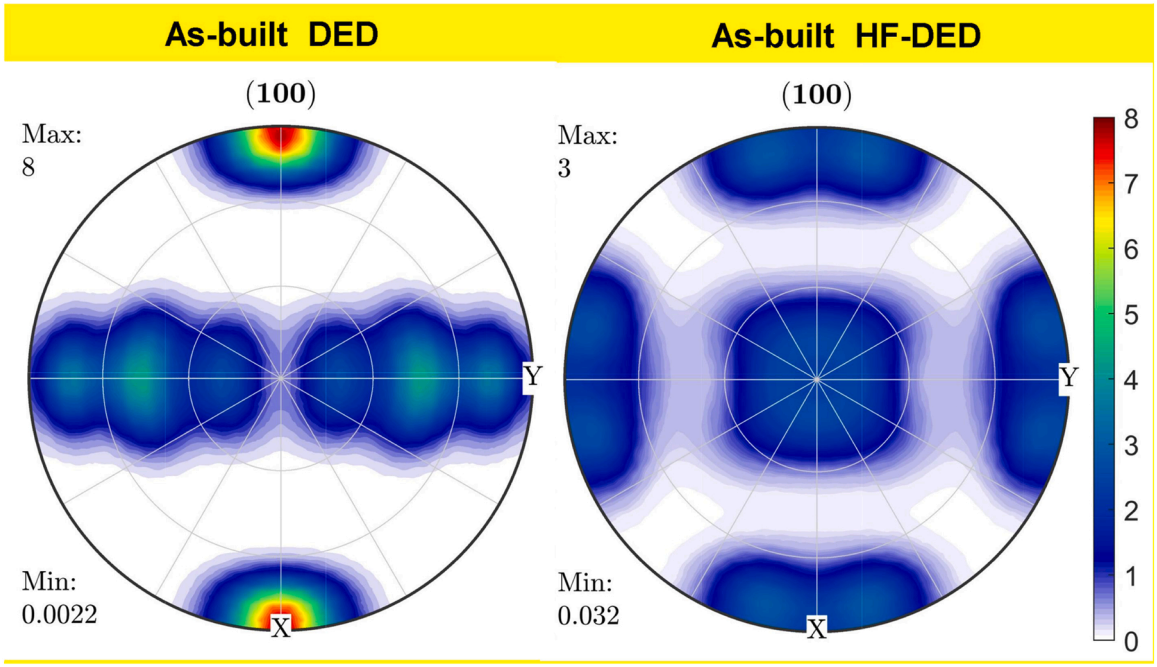

Fig. 9. – Pole figure of the Inconel® 625 arc plasma DEDed and in situ interlayer hot forging DEDed, both in as-built condition.

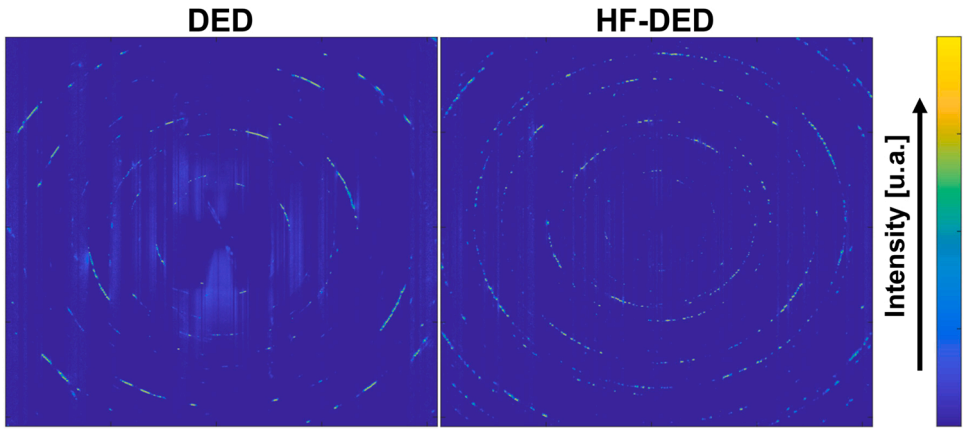

Fig. 10. 2D Debbye-Scherrer diffractions patters of DED and HF-DED materials.

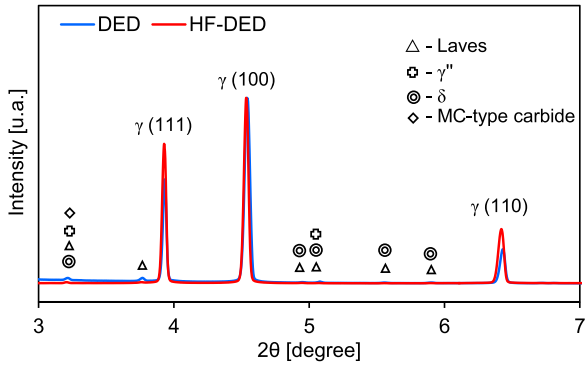

Fig. 11. Synchrotron X-ray diffractogram.

which detailed similar diffraction patterns for both DED and HF-DED. The main observed differences were related to peak intensity, where the HF-DED material showed (111) and (011) γ diffraction peaks with higher intensity (i.e., less oriented) in relation to DED.

According to the experimental solidification model of DuPont et al. [95,96], the Nb-bearing Ni-based superalloys (e.g., Inconel® 625) solidification initiates with the formation of γ and the elemental segregation, especially of Mo, Nb, and C, to the interdendritic liquid. This is followed by the first eutectic reaction (L → γ + MC-type carbide), consuming C, and finishes with the second eutectic reaction (L → γ + Laves). These results were in good agreement with the simulated solidification sequence (previously shown in Fig. 4b), where both MC-type carbides and Laves phase was confirmed by the synchrotron X-ray diffraction (Fig. 11). In addition, Inconel® 625 Scheil-Gulliver solidification simulation predicted the formation of δ. Also, as Van et al. [97] reported, the multiple thermal cycles can induce the solid-state precipitation of δ. As reported by Oh et al. [98] using high-speed in situ synchrotron X-ray diffraction, σ and η phases have not been observed experimentally. This indicates that although these phases are thermodynamically predicted under a solid/liquid local equilibrium condition (Scheil-Gulliver model), the thermal conditions (fast colling rate) during DED suppress their formation. Thus, given the non-significant effect of the in situ interlayer HF variant on solidification conditions concerning the conventional DED [38,58,59], similar

constituents (as shown in Fig. 11), and the maintenance of cube texture component, the main differences between the HF-DED and DED processed materials were related to the remaining thermomechanical-affected zone (Fig. 8c) and the KAM distribution, with high dislocation density in the HF-DED part.

The Vickers microhardness profile (Fig. 12) shows that the HF-DED material had a higher hardness than its DED counterpart. Close to the top bead surface (10th layer), the localized deformation and finer grain size due to dynamic recrystallization induce a significant hardness increase; however, due to the remelting and multiple thermal cycles, the hardness drops from the last layer surface to the substrate direction. The conventional DED material also has a higher hardness in the last layer surface, which was attributed to previously observed CET fine grains (Fig. 6). Throughout the whole part, the HF-DED had a higher hardness than DED, which is related to the remaining deformation (as identified in the KAM map of Fig. 8).

The Inconel® 625 is a solid-solution strengthened Ni-base alloy; thus, considering the non-significant effect of HF-DED on the solidification conditions and phase presents and the Zhang et al. [68] results (solid solution strengthening mechanism did not change for different Inconel® 718 laser powder bed fused conditions), it can be stated that the solid solution strengthening mechanism was similar for both DED and HF-DED conditions. Also, according to Gao et al. [99] and Li et al. [16], the Taylor strengthening (dislocation density) is preponderant in relation to grain boundary strengthening (Hall-Petch relationship) for Inconel® 625, which explains the hardness difference of ≈ 60 $HV_{0.3}$ in the last layer. Given the higher KAM (Fig. 8c; Taylor strengthening) and thin aligned and recrystallized interlayer grains (i.e., finer grain size), a similar analysis can be extended to the remaining part, explaining the higher hardness of HF-DED samples compared to the DED material.

Correlating the hardness profile (Fig. 12) with the HF-DED microstructure (Fig. 6b), it is possible to estimate the total length ($\sim$ 2.1 mm) of the thermo-mechanical-affected zone (dynamically recrystallized grains – $\sim$ 1.2 mm – and deformed primary microstructure – $\sim$ 0.9 mm), which is higher than the subsequent layer penetration ($\sim$ 1.34 mm). Thus, the HF-DED microstructure showed, at the top layer (10th; Fig. 6b), a dynamic recrystallization zone, which is remelted (Fig. 7a), remaining the deformed primary microstructure between the layers (confirmed by the KAM map – Fig. 8e) and some recrystallized grains that originated during the thermal cycles (Fig. 4a). Therefore, the HF-DED produced a deformed microstructure, which can have a potential grain size refinement during annealing heat treatments (see Section 3.3), as observed at cold worked low/medium stacking-fault energy welded materials [100].

3.3. *In situ interlayer hot forging effect on post-deposition heat treatment response*

Given the remaining thermomechanical-affected zone expressed by the KAM distribution (Fig. 8) and the higher hardness of HF-DED condition, the in situ interlayer hot forging can have two distinct grain size refinement mechanisms: in situ (via dynamic recrystallization) and post-process (static recrystallization – during reheating thermal cycles and/or PDHT) [18,36,53–56]. Thus, considering that the in situ grain size refinement was not efficient (completely remelted) to significantly alter the grain morphology and the main crystallographic cube texture (Fig. 8), the present work also sought to improve the grain size refinement via static recrystallization of the remaining thermo-mechanical-affected zone using post-deposition heat treatments (solution and stabilization annealing). HF-DED (980 °C/1 h) and HF-DED (1100 °C/1 h) conditions are denominated as HF-DED-980 and HF-DED-1100, respectively.

Fig. 13 details that the HF-DED-980 material had a significant grain size refinement in relation to as-built DED (61 vs. 375 μm; Fig. 14). However, some aligned non-recrystallized grains persisted. Moreover, the HF-DED-1100 showed a fully equiaxed (recrystallized grains) microstructure with a grain size comparable to wrought material and other arc plasma-DED + interlayer deformation processes (Fig. 14). These results proved that the double grain size refinement mechanisms could occur in Inconel® 625 HF-DEDed, i.e., (i) thin columnar grains and some equiaxed grains can form at the fusion line due to the dynamic recrystallization and (ii) equiaxed grains due to the static recrystallization of the thermomechanical-affected zone during PDHT. Additionally, DED material (typical columnar microstructure; Fig. 13a) had aligned grains (average aspect ratio $>$ 3); PDHT reduced the aligned grains content and promoted equiaxed ones (1 $<$ aspect ratio $<$ 2). Besides, the HF-DED-1100 material had a better heat treatment response than the HF-DED-980 one, which can be related to its higher peak temperature that increased the static recrystallization kinetics and allowed less deformed zones (regions far away from the fusion line) also underwent static recrystallization [89]. In addition, despite the HF-DED-980 material possessing a low texture index (Fig. 8), the solution annealing (HF-DED-1100) eliminated the casting/welding/additive manufacturing typical cube texture (Fig. 13).

Similar to the as-built conditions (DED and HF-DED), the synchrotron X-ray diffraction data (Fig. 15a) did not significantly differ between the HF-DED-980 and HF-DED-1100. However, the intensity of the main γ peaks ({111} and {100}) had a low difference, which is a clear indication of a low cube texture, reinforcing the ODF results (Fig. 13). Also, the KAM distribution (Fig. 15b) indicated that HF-DED-980 had a slightly higher remaining dislocation density (higher median local misorientation), which can be related to the low temperature and time (stabilization annealing – 980 °C/ 1 h) to complete the static recrystallization process. These results matched the hardness profile, which, even considering the HF-DED-1100 finer grain size, reveals that the Taylor strengthening mechanism was preponderant, resulting in a higher ($\sim$ 15 $HV_{0.3}$) hardness of the HF-DED-980 concerning the HF-DED-1100 material. Moreover, comparing the HF-DED-1100 and HF-DED-980 with their DED counterpart (Fig. 16 and Fig. 12, respectively), it is possible to indicate that despite the significant grain size reduction (observed in

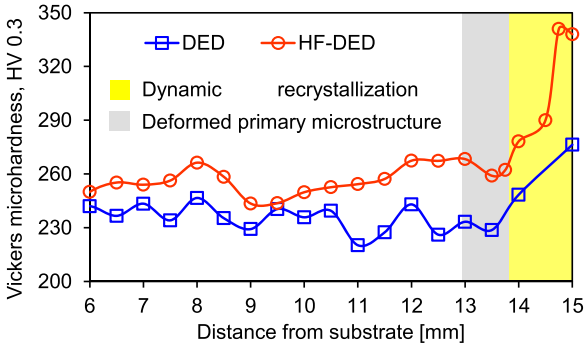

Fig. 12. – Vickers microhardness ($HV_{0.3}$) profiles of the DED and HF-DED materials.

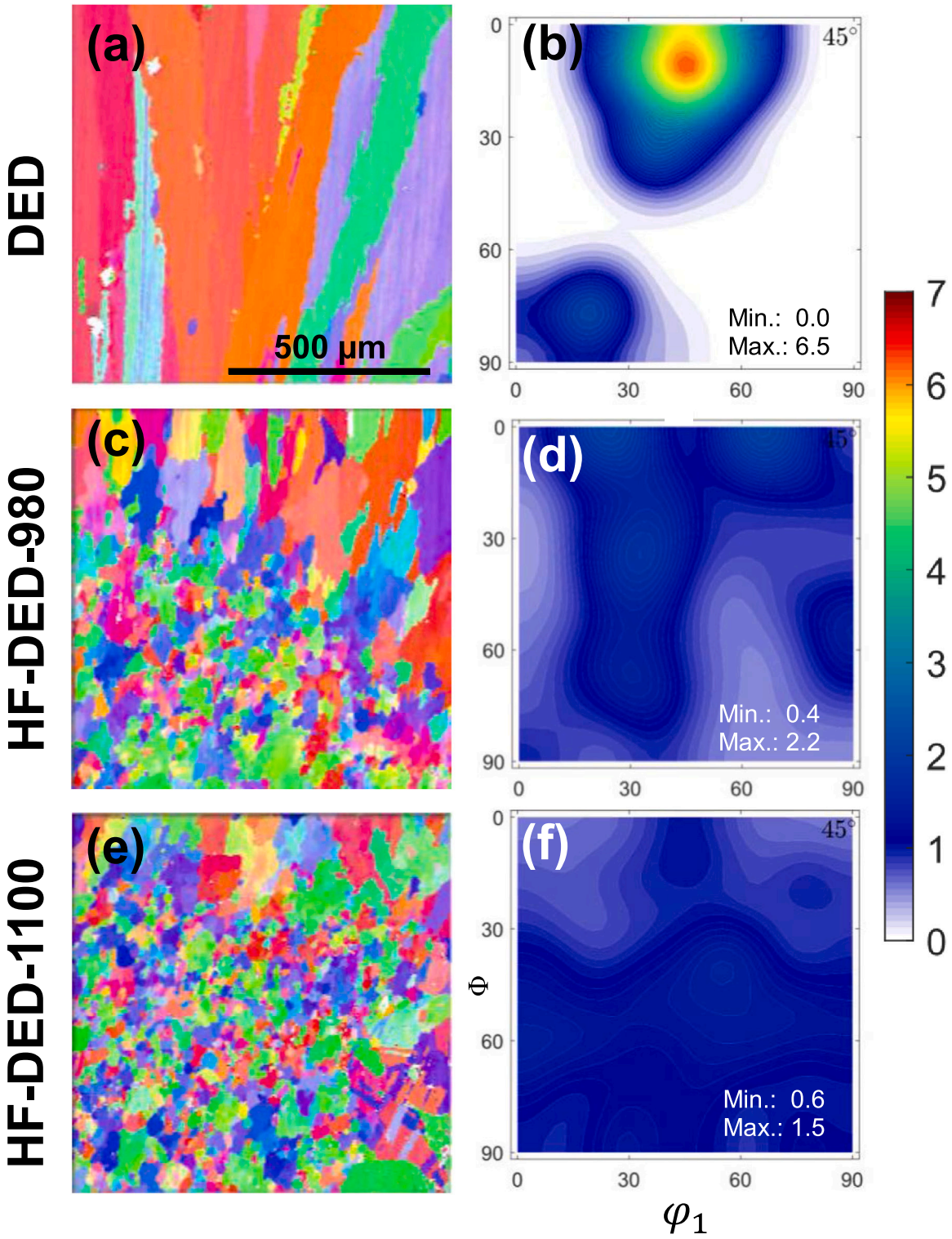

Fig. 13. Electron backscatter diffraction (EBSD) analysis of Inconel® 625 performed at interlayer region: (a) orientation image map (OIM) and (b) orientation distribution function (ODF; $\varphi_2 = 45°$) in DEDed condition; (c) OIM and (d) ODF in HF-DED-980 condition; (e) OIM and (f) ODF in HF-DED-1100 condition. The EBSD data were acquired in the interlayer region, following the Fig. 1c.

Fig. 14), the KAM median of HF-DED-1100 and HF-DED-980 is lower (0.82 and 0.89; Fig. 8c) than that in the DED material (1.19; Fig. 15b), which can explain the DED higher hardness compared to HF-DED-1100 and HF-DED-980 conditions. Therefore, Taylor strengthening mechanism (dislocation density) is superior to the grain boundary for Inconel 625 fabricated via arc plasma DED. The heat treatment reduced the dislocation density and grain size (static recrystallization; Fig. 13). Thus, a concurrent effect occurred: hardness decreases due to the lower dislocation density and increases owing to the smaller grain size. However, among these mechanisms, the dislocation density is preponderant; thus, despite the finer grain size after the heat treatment, the hardness of HF-DED-1100 and HF-DED-980 conditions is lower concerning the as-built DED and HF-DED conditions.

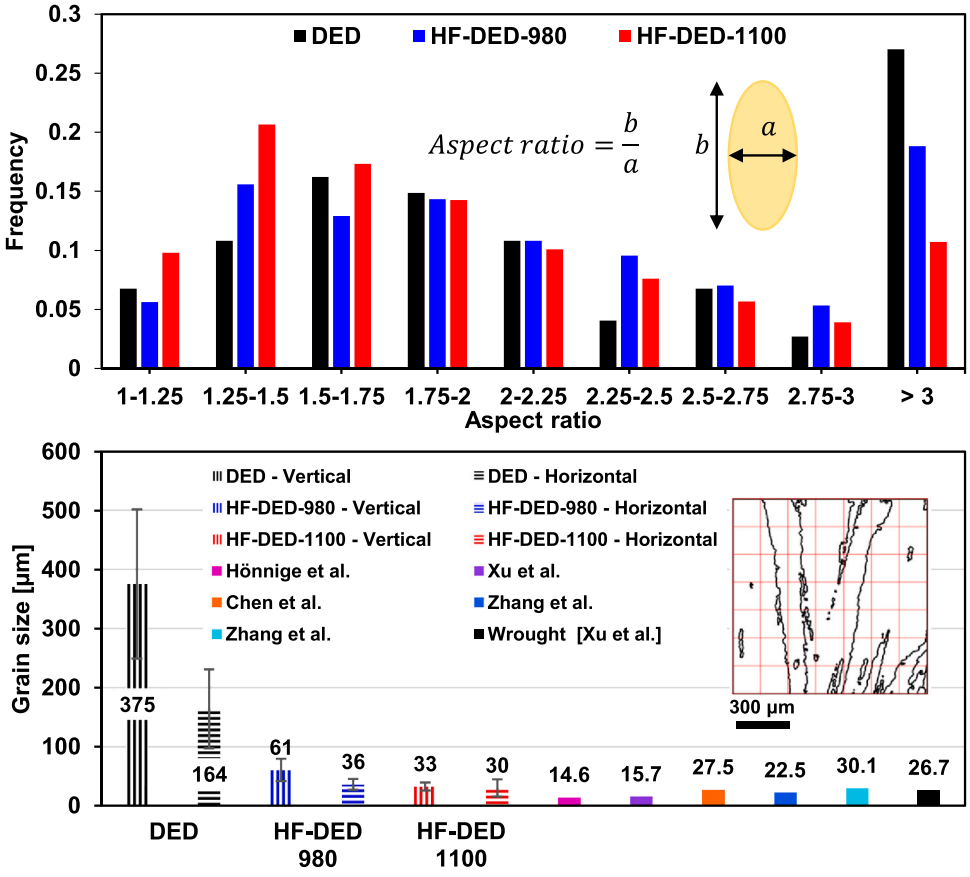

Fig. 14. Grain aspect ratio (upper) and size (bottom) for different Inconel® 625 DED-process conditions. The sub-figures exemplify the aspect ratio calculation and the procedure (intercept method) to measure the grain size, respectively.

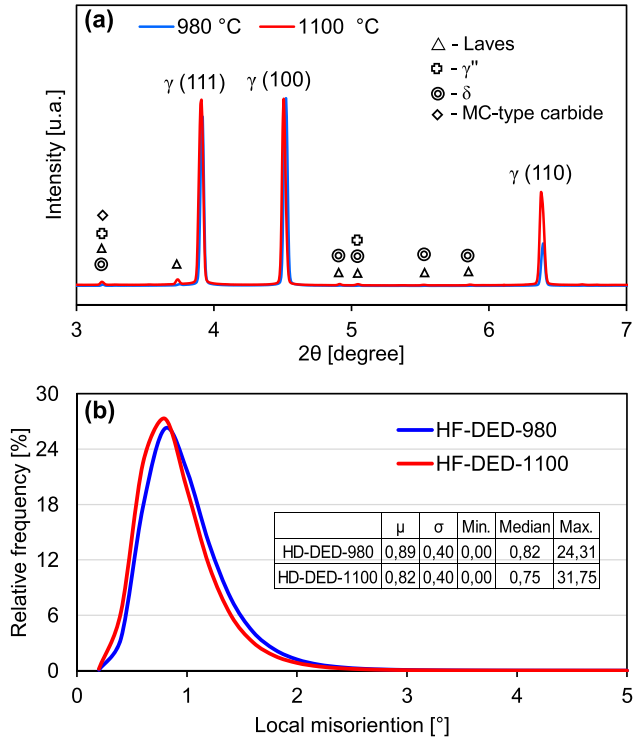

Fig. 15. (a) Synchrotron X-ray diffractogram and (b) Kernel average misorientation distribution calculated from Fig. 13. In (b), μ and σ mean the average and standard error, respectively.

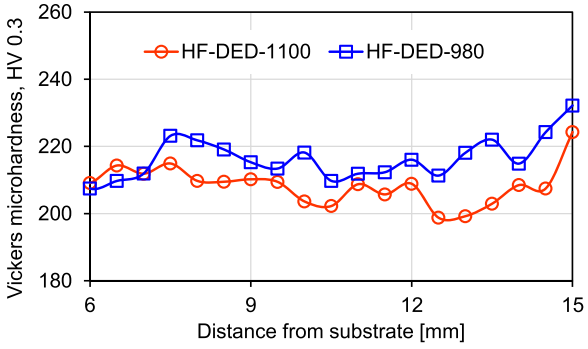

Fig. 16. Vickers microhardness ($HV_{0.3}$) profile for HF-DED-980 and HF-DED-1100 conditions.

4. Conclusions

The present work evaluated the effect of the in situ interlayer hot forging (HF) on the grain size, grain morphology, and crystallographic texture of the Inconel® 625 fabricated via gas metal arc direct energy deposition (DED). Initially, the deformation tool (a circular crown hammer) was designed based on a thermo-metallurgical experimentally validated FEM model. The as-built DED had a typical microstructure (coarse and cube-aligned grains); the HF-DED induced a thermo-mechanical-affected zone (due to dynamic recrystallization) and promoted finer and non-aligned dendrites and some equiaxed grains close to the interlayer fusion line. However, the as-built HF-DED had a low overall effect on the grain size and crystallographic texture. Post-deposition heat treatments (980 °C / 1 h and 1100 °C/ 1 h, following

the ASTM B 446 standard) drove static recrystallization on the thermo-mechanical-affected zone, which promoted a significant change in grain size (from 375 to 30 μm) and grain morphology (majority of equiaxed grain with aspect ratio < 2), eliminating the typical cube texture of Ni-based superalloys additively manufactured. The solution annealing heat treatment (1100 °C/ 1 h) had a more profound effect on the grain size refinement. Therefore, the DED + in situ interlayer hot forging grain size refinement was mainly related to the thermo-mechanical-affected zone static recrystallization during post-deposition heat treatment. In conclusion, DED + in situ interlayer hot forging proved to be a suitable alternative to overcome the coarse and oriented microstructure commonly observed in the Ni-based superalloys obtained by arc plasma-DED.

CRediT authorship contribution statement

Francisco Werley Cipriano Farias – Conceptualization; Data curation; Formal analysis; Investigation; Methodology; Validation; Writing– original draft. **Valdemar R. Duarte** – Conceptualization; Data curation; Formal analysis; Investigation; Methodology; Supervision; Writing– review & editing. **Igor Oliveira Felice** – Formal analysis; Investigation; Writing– review & editing. **João da Cruz Payão Filho** – Software; Validation. **Norbert Schell** – Investigation; Resources. **Emad Maawad** – Investigation. **J. A. Avila** –Investigation. **J. Y. Li** – Data curation; Investigation. **Y. Zhang** – Data curation; Investigation. **T. G. Santos** – Conceptualization; Data curation; Formal analysis; Funding acquisition; Investigation; Methodology; Project administration; Resources; Supervision; Visualization; Writing– review & editing. **J. P. Oliveira** – Conceptualization; Data curation; Formal analysis; Funding acquisition; Investigation; Methodology; Project administration; Resources; Supervision; Visualization; Writing– review & editing.

Declaration of Competing Interest

The authors declare that they have no known competing financial interests or personal relationships that could have appeared to influence the work reported in this paper.

Data Availability

No data was used for the research described in the article.

Acknowledgments

Authors acknowledge the Portuguese Fundação para a Ciência e a Tecnologia (FCT – MCTES), Portugal, for its financial support via the project UID/EMS/00667/2019 (UNIDEMI). JPO acknowledges funding by national funds from FCT - Fundação para a Ciência e a Tecnologia, Portugal, I.P., in the scope of the projects LA/P/0037/2020, UIDP/50025/2020 and UIDB/50025/2020 of the Associate Laboratory Institute of Nanostructures, Nanomodelling and Nanofabrication – i3N. FWCF acknowledges Fundação para a Ciência e a Tecnologia (FCT-MCTES), Portugal, for funding the Ph.D. Grant 2022.13870. BD. The authors acknowledge DESY (Hamburg, Germany), a member of the Helmholtz Association HGF, for the provision of experimental facilities. Beamtime was allocated for proposal I-20210986 EC. The research leading to this result has been supported by the project CALIPSOplus under the Grant Agreement 730872 from the EU Framework Programme for Research and Innovation HORIZON 2020. This activity has received funding from the European Institute of Innovation and Technology (EIT) Raw Materials through the project Smart WAAM: Microstructural Engineering and Integrated Non-Destructive Testing. YZ acknowledges the National Natural Science Foundation of China (51601091), the Natural Science Foundation of Jiangsu Province (BK 20160826), the Six Talent Peaks Project of Jiangsu Province (2017-XCL-051), the Fundamental Research Funds for the Central Universities (30917011106), and Key Research and Development Plan of Jiangsu Province (BE 2020085).

References

[1] S.W. Williams, F. Martina, A.C. Addison, J. Ding, G. Pardal, P. Colegrove, Wire + arc additive manufacturing, Mater. Sci. Technol. 32 (2016) 641–647, https://doi.org/10.1179/1743284715Y.0000000073.

[2] N. Kumar, H. Bhavsar, P.V.S. Mahesh, A.K. Srivastava, B.J. Bora, A. Saxena, A. R. Dixit, Wire arc additive manufacturing – a revolutionary method in additive manufacturing, Mater. Chem. Phys. 285 (2022), 126144, https://doi.org/10.1016/j.matchemphys.2022.126144.

[3] T.A. Rodrigues, V. Duarte, R.M. Miranda, T.G. Santos, J.P. Oliveira, Current status and perspectives on wire and arc additive manufacturing (WAAM), Mater 12 (2019) 1121, https://doi.org/10.3390/ma12071121.

[4] P.P. Fonseca, C. Vidal, F. Ferreira, V.R. Duarte, T.A. Rodrigues, T.G. Santos, C. M. Machado, Orthogonal cutting of wire and arc additive manufactured parts, Int. J. Adv. Manuf. Technol. 119 (2022) 4439–4459, https://doi.org/10.1007/s00170-022-08678-3.

[5] Y. Yehorov, L.J. da Silva, A. Scotti, Balancing WAAM production costs and wall surface quality through parameter selection: a case study of an Al-Mg5 alloy multilayer-non-oscillated single pass wall, J. Manuf. Mater. Process 3 (2019), https://doi.org/10.3390/jmmp3020032.

[6] H. Zhang, C. Huang, G. Wang, R. Li, G. Zhao, Comparison of energy consumption between hybrid deposition & micro-rolling and conventional approach for wrought parts, J. Clean. Prod. 279 (2021), 123307, https://doi.org/10.1016/j.jclepro.2020.123307.

[7] J. Moor, A. Debiccari, B. Lagow, S. Tewari, M. Kinsella, Additive manufacturing for superalloys – producibility and cost, in: 7th Int. Symp. Superalloys 718 Deriv., TMS, The Minerals, Metals & Materials Society, 2010, pp. 521–537, https://doi.org/10.1002/9781118495223.ch40.

[8] C.L. English, S.K. Tewari, D.H. Abbott, An overview of ni base additive fabrication technologies for aerospace applications, in: 7th Int. Symp. Superalloy 718 Deriv. 2010, TMS, The Minerals, Metals & Materials Society, 2010, pp. 399–412, https://doi.org/10.1002/9781118495223.ch31.

[9] B.O. Omiyale, T.O. Olugbade, T.E. Abioye, P.K. Farayibi, Wire arc additive manufacturing of aluminium alloys for aerospace and automotive applications: a review, Mater. Sci. Technol. 38 (2022) 391–408, https://doi.org/10.1080/02670836.2022.2045549.

[10] C.R. Cunningham, S. Wikshåland, F. Xu, N. Kemakolam, A. Shokrani, V. Dhokia, S.T. Newman, Cost modelling and sensitivity analysis of wire and arc additive manufacturing, Procedia Manuf. 11 (2017) 650–657, https://doi.org/10.1016/j.promfg.2017.07.163.

[11] P. Raval, D. Patel, R. Prajapati, V. Badheka, M.K. Gupta, N. Khanna, Energy consumption and economic modelling of performance measures in machining of wire arc additively manufactured Inconel-625, Sustain. Mater. Technol. 32 (2022), e00434, https://doi.org/10.1016/j.susmat.2022.e00434.

[12] I. Sirichakwal, B. Conner, Implications of additive manufacturing for spare parts inventory, 3D Print. Addit. Manuf. 3 (2016) 56–63, https://doi.org/10.1089/3dp.2015.0035.

[13] A. Gamon, E. Arrieta, P.R. Gradl, C. Katsarelis, L.E. Murr, R.B. Wicker, F. Medina, Microstructure and hardness comparison of as-built inconel 625 alloy following various additive manufacturing processes, Results Mater. 12 (2021), 100239, https://doi.org/10.1016/j.rinma.2021.100239.

[14] A. Chintala, M. Tejaswi Kumar, M. Sathishkumar, N. Arivazhagan, M. Manikandan, Technology development for producing inconel 625 in aerospace application using wire arc additive manufacturing process, J. Mater. Eng. Perform. 30 (2021) 5333–5341, https://doi.org/10.1007/s11665-021-05781-6.

[15] W. Yangfan, C. Xizhang, S. Chuanchu, Microstructure and mechanical properties of Inconel 625 fabricated by wire-arc additive manufacturing, Surf. Coat. Technol. 374 (2019) 116–123, https://doi.org/10.1016/j.surfcoat.2019.05.079.

[16] S. Li, J.Y. Li, Z.W. Jiang, Y. Cheng, Y.Z. Li, S. Tang, J.Z. Leng, H.X. Chen, Y. Zou, Y.H. Zhao, J.P. Oliveira, Y. Zhang, K.H. Wang, Controlling the columnar-to-equiaxed transition during directed energy deposition of inconel 625, Addit. Manuf. 57 (2022), https://doi.org/10.1016/j.addma.2022.102958.

[17] X. Yuan, H. Qiu, F. Zeng, W. Luo, H. Li, X. Wang, N. Guan, F. Cui, Microstructural evolution and mechanical properties of Inconel 625 superalloy fabricated by pulsed microplasma rapid additive manufacturing, J. Manuf. Process 77 (2022) 63–74, https://doi.org/10.1016/j.jmapro.2022.03.008.

[18] J. Hönnige, C.E. Seow, S. Ganguly, X. Xu, S. Cabeza, H. Coules, S. Williams, Study of residual stress and microstructural evolution in as-deposited and inter-pass rolled wire plus arc additively manufactured Inconel 718 alloy after ageing treatment, Mater. Sci. Eng. A 801 (2021), https://doi.org/10.1016/j.msea.2020.140368.

[19] C.E. Seow, H. Coules, R. Khan, Effect of crack orientation on fracture behaviour of wire + arc additively manufactured (WAAM) nickel-base superalloy, in: Vessel. Pip. Conf., ASME, 2018, pp. 1–9, https://doi.org/10.1115/PVP2018-84090.

[20] A.N.M. Tanvir, M.R.U. Ahsan, G. Seo, J. duk Kim, C. Ji, B. Bates, Y. Lee, D.B. Kim, Heat treatment effects on Inconel 625 components fabricated by wire + arc additively manufacturing (WAAM)—part 2: mechanical properties, Int. J. Adv. Manuf. Technol. 110 (2020) 1709–1721, https://doi.org/10.1007/s00170-020-05980-w.

[21] A. Safarzade, M. Sharifitabar, M.A. Shafiee, Effects of heat treatment on microstructure and mechanical properties of Inconel 625 alloy fabricated by wire arc additive manufacturing process, Trans. Nonferrous Met. Soc. China 30 (2020) 3016–3030, https://doi.org/10.1016/S1003-6326(20)65439-5.

[22] A.N.M. Tanvir, M.R.U. Ahsan, C. Ji, W. Hawkins, B. Bates, Duck, B. Kim, Heat treatment effects on Inconel 625 components fabricated by wire + arc additive manufacturing (WAAM)-part 1: microstructural characterization, Int. J. Adv. Manuf. Technol. 103 (2019) 3785–3798, https://doi.org/10.1007/s00170-019-03828-6.

[23] R.K. Mookara, S. Seman, R. Jayaganthan, M. Amirthalingam, Influence of droplet transfer behaviour on the microstructure, mechanical properties and corrosion resistance of wire arc additively manufactured Inconel (IN) 625 components, Weld. World 65 (2021) 573–588, https://doi.org/10.1007/s40194-020-01043-6.

[24] Q. Jiang, P. Zhang, Z. Yu, H. Shi, S. Li, D. Wu, H. Yan, X. Ye, J. Chen, Microstructure and mechanical properties of thick-walled inconel 625 alloy manufactured by wire arc additive manufacture with different torch paths, Adv. Eng. Mater. 23 (2021) 2000728, https://doi.org/10.1002/ADEM.202000728.

[25] G. Singh Rajput, M. Gor, H. Soni, V. Badheka, P. Sahlot, Effect of deposition strategies on mechanical strength of wire arc additively manufactured Inconel 625, Mater. Today Proc. 62 (2022) 7324–7328, https://doi.org/10.1016/j.matpr.2022.05.164.

[26] Y. Wang, X. Chen, Investigation on the microstructure and corrosion properties of Inconel 625 alloy fabricated by wire arc additive manufacturing, Mater. Res. Express 6 (2019), 106568, https://doi.org/10.1088/2053-1591/ab39f6.

[27] F. Xu, Y. Lv, Y. Liu, F. Shu, P. He, B. Xu, Microstructural evolution and mechanical properties of inconel 625 alloy during pulsed plasma arc deposition process, J. Mater. Sci. Technol. 29 (2013) 480–488, https://doi.org/10.1016/j.jmst.2013.02.010.

[28] X. Wang, Q. Hu, T. Li, W. Liu, D. Tang, Z. Hu, K. Liu, Microstructure and fracture performance of wire arc additively manufactured inconel 625 alloy by hot-Wire GTAW, Metals (Basel) 12 (2022) 1–10, https://doi.org/10.3390/met12030510.

[29] W. Kurz, C. Bezençon, M. Gäumann, Columnar to equiaxed transition in solidification processing, Sci. Technol. Adv. Mater. 2 (2001) 185–191, https://doi.org/10.1016/S1468-6996(01)00047-X.

[30] R. Motallebi, Z. Savaedi, H. Mirzadeh, Additive manufacturing – a review of hot deformation behavior and constitutive modeling of flow stress, Curr. Opin. Solid State Mater. Sci. 26 (2022), 100992, https://doi.org/10.1016/j.cossms.2022.100992.

[31] S.A. Nabavizadeh, M. Eshraghi, S.D. Felicelli, Three-dimensional phase field modeling of columnar to equiaxed transition in directional solidification of Inconel 718 alloy, J. Cryst. Growth 549 (2020), 125879, https://doi.org/10.1016/J.JCRYSGRO.2020.125879.

[32] J.J. Debarbadillo, S.K. Mannan, Alloy 718 for oilfield applications, JOM 64 (2012) 265–270, https://doi.org/10.1007/s11837-012-0238-z.

[33] Y. Chen, M. Xu, T. Zhang, J. Xie, K. Wei, S. Wang, L. Yin, P. He, Grain refinement and mechanical properties improvement of Inconel 625 alloy fabricated by ultrasonic-assisted wire and arc additive manufacturing, J. Alloy. Compd. 910 (2022), 164957, https://doi.org/10.1016/j.jallcom.2022.164957.

[34] Q. Ma, H. Chen, N. Ren, Y. Zhang, L. Hu, W. Meng, X. Yin, Effects of ultrasonic vibration on microstructure, mechanical properties, and fracture mode of inconel 625 parts fabricated by cold metal transfer arc additive manufacturing, J. Mater. Eng. Perform. 30 (2021) 6808–6820, https://doi.org/10.1007/s11665-021-06023-5.

[35] Y. Wang, X. Chen, Q. Shen, C. Su, Y. Zhang, S. Jayalakshmi, R.A. Singh, Effect of magnetic field on the microstructure and mechanical properties of inconel 625 superalloy fabricated by wire arc additive manufacturing, J. Manuf. Process 64 (2021) 10–19, https://doi.org/10.1016/j.jmapro.2021.01.008.

[36] C. Li, Y. Tian, Y. Chen, P. Hodgson, X. Wu, Y. Zhu, A. Huang, Hierarchical layered and refined grain structure of Inconel 718 superalloy produced by rolling-assisted directed energy deposition, Addit. Manuf. Lett. 1 (2021), 100009, https://doi.org/10.1016/j.addlet.2021.100009.

[37] X. Xu, S. Ganguly, J. Ding, P. Dirisu, F. Martina, X. Liu, S.W. Williams, Improving mechanical properties of wire plus arc additively manufactured maraging steel through plastic deformation enhanced aging response, Mater. Sci. Eng. A 747 (2019) 111–118, https://doi.org/10.1016/j.msea.2018.12.114.

[38] V.R. Duarte, T.A. Rodrigues, N. Schell, R.M. Miranda, J.P. Oliveira, T.G. Santos, Hot forging wire and arc additive manufacturing (HF-WAAM), Addit. Manuf. 35 (2020), 101193, https://doi.org/10.1016/j.addma.2020.101193.

[39] B. Wu, Z. Pan, D. Ding, D. Cuiuri, H. Li, Z. Fei, The effects of forced interpass cooling on the material properties of wire arc additively manufactured Ti6Al4V alloy, J. Mater. Process. Technol. 258 (2018) 97–105, https://doi.org/10.1016/j.jmatprotec.2018.03.024.

[40] T.A. Rodrigues, V.R. Duarte, D. Tomás, J.A. Avila, J.D. Escobar, E. Rossinyol, N. Schell, T.G. Santos, J.P. Oliveira, In-situ strengthening of a high strength low alloy steel during Wire and Arc Additive Manufacturing (WAAM), Addit. Manuf. 34 (2020), 101200, https://doi.org/10.1016/j.addma.2020.101200.

[41] D. Kong, C. Dong, X. Ni, L. Zhang, C. Man, J. Yao, Y. Ji, Y. Ying, K. Xiao, X. Cheng, X. Li, High-throughput fabrication of nickel-based alloys with different Nb contents via a dual-feed additive manufacturing system: Effect of Nb content on microstructural and mechanical properties, J. Alloy. Compd. 785 (2019) 826–837, https://doi.org/10.1016/J.JALLCOM.2019.01.263.

[42] P.A. Colegrove, H.E. Coules, J. Fairman, F. Martina, T. Kashoob, H. Mamash, L. D. Cozzolino, Microstructure and residual stress improvement in wire and arc additively manufactured parts through high-pressure rolling, J. Mater. Process. Technol. 213 (2013) 1782–1791, https://doi.org/10.1016/j.jmatprotec.2013.04.012.

[43] C. Liu, J. Yang, Q. Ge, F. Gao, J. Zou, Mechanical properties improvement of thick multi-pass weld by layered ultrasonic impact treatment, Sci. Technol. Weld. Join. 23 (2018) 95–104, https://doi.org/10.1080/13621718.2017.1327201.

[44] T.E. Adams, S. Härtel, A. Hälsig, B. Awiszus, P. Mayr, WeldForming: a new inline process combination to improve weld seam properties, Weld. World 64 (2020) 601–610, https://doi.org/10.1007/s40194-020-00856-9.

[45] W. Liu, X. Tian, X. Zhang, Preventing weld hot cracking by synchronous rolling during welding, Weld. J. 75 (1996) 297s–304s.

[46] H.E. Coules, P. Colegrove, L.D. Cozzolino, S.W. Wen, S. Ganguly, T. Pirling, Effect of high pressure rolling on weld-induced residual stresses, Sci. Technol. Weld. Join. 17 (2012) 394–401, https://doi.org/10.1179/1362171812Y.0000000021.

[47] P. Sokolov, A. Aleshchenko, A. Koshmin, V. Cheverikin, P. Petrovskiy, A. Travyanov, A. Sova, Effect of hot rolling on structure and mechanical properties of Ti-6Al-4V alloy parts produced by direct laser deposition, Int. J. Adv. Manuf. Technol. 107 (2020) 1595–1603, https://doi.org/10.1007/s00170-020-05132-0.

[48] Y. Zhou, X. Lin, N. Kang, Z. Wang, H. Tan, W. Huang, Hot deformation induced microstructural evolution in local-heterogeneous wire + arc additive manufactured 2219 Al alloy, J. Alloy. Compd. 865 (2021), 158949, https://doi.org/10.1016/j.jallcom.2021.158949.

[49] J. Chen, H. Wei, X. Zhang, Y. Peng, J. Kong, K. Wang, Flow behavior and microstructure evolution during dynamic deformation of 316 L stainless steel fabricated by wire and arc additive manufacturing, Mater. Des. 198 (2021), 109325, https://doi.org/10.1016/j.matdes.2020.109325.

[50] B. Lan, Y. Wang, Y. Liu, P. Hooper, C. Hopper, G. Zhang, X. Zhang, J. Jiang, The influence of microstructural anisotropy on the hot deformation of wire arc additive manufactured (WAAM) Inconel 718, Mater. Sci. Eng. A 823 (2021), 141733, https://doi.org/10.1016/j.msea.2021.141733.

[51] W. Zhao, G.C. Zha, M.Z. Xi, S.Y. Gao, Effects of synchronous rolling on microstructure, hardness, and wear resistance of laser multilayer cladding, J. Mater. Eng. Perform. 27 (2018) 1746–1752, https://doi.org/10.1007/s11665-018-3286-x.

[52] Q. Li, Y. Zhang, J. Chen, B. Guo, W. Wang, Y. Jing, Y. Liu, Effect of ultrasonic micro-forging treatment on microstructure and mechanical properties of GH3039 superalloy processed by directed energy deposition, J. Mater. Sci. Technol. 70 (2021) 185–196, https://doi.org/10.1016/j.jmst.2020.09.001.

[53] X. Xu, S. Ganguly, J. Ding, C.E. Seow, S. Williams, Enhancing mechanical properties of wire + arc additively manufactured INCONEL 718 superalloy through in-process thermomechanical processing, Mater. Des. 160 (2018) 1042–1051, https://doi.org/10.1016/j.matdes.2018.10.038.

[54] T. Zhang, H. Li, H. Gong, J. Ding, Y. Wu, C. Diao, X. Zhang, S. Williams, Hybrid wire - arc additive manufacture and effect of rolling process on microstructure and tensile properties of Inconel 718, J. Mater. Process. Technol. 299 (2022), 117361, https://doi.org/10.1016/j.jmatprotec.2021.117361.

[55] Q. Chen, G. Wang, H. Zhang, R. Li, Research on microstructure and mechanical properties of hybrid plasma arc and micro-rolling additive manufacturing of Inconel 718 superalloy, Rapid Prototyp. J. (2022), https://doi.org/10.1108/rpj-09-2021-0227.

[56] Y. Wang, J. Shi, Recrystallization behavior and tensile properties of laser metal deposited Inconel 718 upon in-situ ultrasonic impact peening and heat treatment, Mater. Sci. Eng. A. 786 (2020), 139434, https://doi.org/10.1016/j.msea.2020.139434.

[57] J.R. Hönnige, P. Colegrove, S. Williams, Improvement of microstructure and mechanical properties in Wire + Arc additively manufactured Ti-6Al-4V with machine hammer peening, Procedia Eng. 216 (2017) 8–17, https://doi.org/10.1016/j.proeng.2018.02.083.

[58] V.R. Duarte, T.A. Rodrigues, N. Schell, R.M. Miranda, J.P. Oliveira, T.G. Santos, In-situ hot forging direct energy deposition-arc of CuAl8 alloy, Addit. Manuf. (2022), 102847, https://doi.org/10.1016/j.addma.2022.102847.

[59] V.R. Duarte, Developments in directed energy deposition additive manufacturing: In-situ Hot Forging and Indirect Cooling, Univ. NOVA De. Lisb. (2022). ⟨https://run.unl.pt/handle/10362/134198⟩. accessed April 19, 2022.

[60] C.E. Seow, H.E. Coules, G. Wu, R.H.U. Khan, X. Xu, S. Williams, Wire + arc additively manufactured inconel 718: effect of post-deposition heat treatments on microstructure and tensile properties, Mater. Des. 183 (2019), 108157, https://doi.org/10.1016/j.matdes.2019.108157.

[61] L.M.B. de Azevedo, A.R. Figueiredo, F. da Cruz Gallo, L.S. Araújo, F.W.C. Farias, R. da Silva Teixeira, T.M. Ivaniski, L.H. de Almeida, M.C. Mendes, Effects of different wire drawing routes on grain boundary character distribution, microtexture, δ-phase precipitation, grain size and room temperature mechanical behavior of alloy 718, Mater. Res. 23 (2020) 20200131, https://doi.org/10.1590/1980-5373-MR-2020-0131.

[62] R. Lackner, G. Mori, R. Egger, F. Winter, M. Albu, W. Grogger, Sensitization of as rolled and stable annealed alloy 625, BHM Berg. - Und Hüttenmännische Mon. 159 (2014) 12–22, https://doi.org/10.1007/s00501-013-0225-x.

[63] N. Xi, X. Fang, Y. Duan, Q. Zhang, K. Huang, Wire arc additive manufacturing of Inconel 718: constitutive modelling and its microstructure basis, J. Manuf. Process 75 (2022) 1134–1143, https://doi.org/10.1016/j.jmapro.2022.01.067.

[64] G. Ravi, N. Murugan, R. Arulmani, Microstructure and mechanical properties of Inconel-625 slab component fabricated by wire arc additive manufacturing, Mater. Sci. Technol. 36 (2020) 1785–1795, https://doi.org/10.1080/02670836.2020.1836737.

[65] Y.L. Hu, X. Lin, S.Y. Zhang, Y.M. Jiang, X.F. Lu, H.O. Yang, W.D. Huang, Effect of solution heat treatment on the microstructure and mechanical properties of Inconel 625 superalloy fabricated by laser solid forming, J. Alloy. Compd. 767 (2018) 330–344, https://doi.org/10.1016/j.jallcom.2018.07.087.

[66] Y. Hu, X. Lin, Y. Li, S. Zhang, Q. Zhang, W. Chen, W. Li, W. Huang, Influence of heat treatments on the microstructure and mechanical properties of Inconel 625

fabricated by directed energy deposition, Mater. Sci. Eng. A. 817 (2021), 141309, https://doi.org/10.1016/j.msea.2021.141309.
[67] R. Hielscher, H. Schaeben, A novel pole figure inversion method: specification of the MTEX algorithm, J. Appl. Crystallogr. 41 (2008) 1024–1037, https://doi.org/10.1107/S0021889808030112.
[68] S. Zhang, X. Lin, L. Wang, X. Yu, Y. Hu, H. Yang, L. Lei, W. Huang, Strengthening mechanisms in selective laser-melted Inconel718 superalloy, Mater. Sci. Eng. A. 812 (2021), 141145, https://doi.org/10.1016/j.msea.2021.141145.
[69] T.A. Rodrigues, J.D. Escobar, J. Shen, V.R. Duarte, G.G. Ribamar, J.A. Avila, E. Maawad, N. Schell, T.G. Santos, J.P. Oliveira, Effect of heat treatments on 316 stainless steel parts fabricated by wire and arc additive manufacturing: Microstructure and synchrotron X-ray diffraction analysis, Addit, Manuf 48 (2021), 102428, https://doi.org/10.1016/j.addma.2021.102428.
[70] L. Karlsson, J. Goldak, Computational welding mechanics, in: R.B. Hetnarski (Ed.), Encycl. Therm. Stress., Springer Netherlands, Dordrecht, 2014, pp. 630–637, https://doi.org/10.1007/978-94-007-2739-7_437.
[71] J.M. Bergheau, R. Fortunier, Finite Element Simulation of Heat Transfer, Wiley-ISTE,, 2010, https://doi.org/10.1002/9780470611418.
[72] J. Goldak, A. Chakravarti, M. Bibby, A new finite element model for welding heat sources, Metall. Trans. B 15 (1984) 299–305, https://doi.org/10.1007/BF02667333.
[73] F.W.C. Farias, J. da, C. Payão Filho, V.H.P. Moraes e Oliveira, Prediction of the interpass temperature of a wire arc additive manufactured wall: FEM simulations and artificial neural network, Addit. Manuf. 48 (2021), 102387, https://doi.org/10.1016/j.addma.2021.102387.
[74] K.P. Prajadhiama, Y.H. Manurung, Z. Minggu, F.H. Pengadau, M. Graf, A. Haelsig, T.-E. Adams, H. Leng Choo, H.L. Choo, Development of bead modelling for distortion analysis induced by wire arc additive manufacturing using FEM and experiment, MATEC Web Conf. (2019) 05003, https://doi.org/10.1051/matecconf/201926905003.
[75] F.E. Bock, J. Herrnring, M. Froend, J. Enz, N. Kashaev, B. Klusemann, Experimental and numerical thermo-mechanical analysis of wire-based laser metal deposition of Al-Mg alloys, J. Manuf. Process 64 (2021) 982–995, https://doi.org/10.1016/j.jmapro.2021.02.016.
[76] S.A. Tsirkas, Numerical simulation of the laser welding process for the prediction of temperature distribution on welded aluminium aircraft components, Opt. Laser Technol. 100 (2018) 45–56, https://doi.org/10.1016/j.optlastec.2017.09.046.
[77] P. Henckell, M. Gierth, Y. Ali, J. Reimann, J.P. Bergmann, Reduction of energy input in wire arc additive manufacturing (WAAM) with gas metal arc welding (GMAW), Mater. (Basel) 13 (2020) 2491, https://doi.org/10.3390/ma13112491.
[78] C. Heinze, C. Schwenk, M. Rethmeier, J. Caron, Numerical sensitivity analysis of welding-induced residual stress depending on variations in continuous cooling transformation behavior, Front. Mater. Sci. 5 (2011) 168–178, https://doi.org/10.1007/s11706-011-0131-7.
[79] S.S. Sandes, C.P. Alvarães, M.C. Mendes, L.S. de Araújo, L.F.G. de Souza, J.C. F. Jorge, Avaliação de Revestimentos de Liga de Níquel 625 Depositados pelo Processo Eletroescória, Soldag. Insp. 21 (2017) 417–427, https://doi.org/10.1590/0104-9224/SI2104.03.
[80] J.N. DuPont, J.C. Lippold, S.D. Kiser. Welding Metallurgy and Weldability of Nickel-Base Alloys, 1st ed., John Wiley & Sons, Inc,, 2009 https://doi.org/10.1002/9780470500262.
[81] M.J. Cieslak, T.J. Headley, T. Kollie, A.D. Romig, A melting and solidification study of alloy 625, Metall. Trans. A 19 (1988) 2319–2331, https://doi.org/10.1007/BF02645056.
[82] H. Zhang, X. Wang, G. Wang, Y. Zhang, Hybrid direct manufacturing method of metallic parts using deposition and micro continuous rolling, Rapid Prototyp. J. 19 (2013) 387–394, https://doi.org/10.1108/RPJ-01-2012-0006.
[83] N. Coniglio, C.E. Cross, Initiation and growth mechanisms for weld solidification cracking, Int. Mater. Rev. 58 (2013) 375–397, https://doi.org/10.1179/1743280413Y.0000000020.
[84] D. Li, Q. Guo, S. Guo, H. Peng, Z. Wu, The microstructure evolution and nucleation mechanisms of dynamic recrystallization in hot-deformed Inconel 625 superalloy, Mater. Des. 32 (2011) 696–705, https://doi.org/10.1016/j.matdes.2010.07.040.
[85] J. Yu, D. Wang, J. Chen, C. Yang, X. Hao, J. Zhou, D. Li, D. Shu, C. Xiao, Y. Peng, High temperature behaviors of a casting nickel-based superalloy used for 815 °C, Mater. (Basel) 14 (2021) 716, https://doi.org/10.3390/ma14040716.
[86] M. Gäumann, C. Bezençon, P. Canalis, W. Kurz, Single-crystal laser deposition of superalloys: processing–microstructure maps, Acta Mater. 49 (2001) 1051–1062, https://doi.org/10.1016/S1359-6454(00)00367-0.
[87] F.W.C. Farias, J. da, C. Payão Filho, D.A. da Silva Júnior, R.N. de Moura, M.C. G. Rios, Microstructural characterization of Ni-based superalloy 625 clad welded on a 9% Ni steel pipe by plasma powder transferred arc, Surf. Coat. Technol. 374 (2019) 1024–1037, https://doi.org/10.1016/j.surfcoat.2019.06.084.
[88] Y. Wang, J. Shi, Microstructure and properties of inconel 718 fabricated by directed energy deposition with in-situ ultra, Sonic Impact Peen., Metall. Mater. Trans. B Process. Metall. Mater. Process. Sci. 50 (2019) 2815–2827, https://doi.org/10.1007/s11663-019-01672-3.
[89] A. Rollett, F. Humphreys, G.S. Rohrer, M. Hatherly. Recrystallization and Related Annealing Phenomena, 2nd ed., Elsevier Ltd, 2004 https://doi.org/10.1016/B978-0-08-044164-1.X5000-2.
[90] S. Kou. Welding Metallurgy, 2nd ed., John Wiley & Sons, Inc, 2002 https://doi.org/10.1002/0471434027.
[91] M. Gustafsson, M. Thuvander, E.L. Bergqvist, E. Keehan, L. Karlsson, Effect of welding procedure on texture and strength of nickel based weld metal, Sci. Technol. Weld. Join. 12 (2013) 549–555, https://doi.org/10.1179/174329307×213800.
[92] A. Eghlimi, M. Shamanian, M. Eskandarian, A. Zabolian, M. Nezakat, J. A. Szpunar, Evaluation of microstructure and texture across the welded interface of super duplex stainless steel and high strength low alloy steel, Surf. Coat. Technol. 264 (2015) 150–162, https://doi.org/10.1016/j.surfcoat.2014.12.060.
[93] Q. Liu, D. Juul Jensen, N. Hansen, Effect of grain orientation on deformation structure in cold-rolled polycrystalline aluminium, Acta Mater. 46 (1998) 5819–5838, https://doi.org/10.1016/S1359-6454(98)00229-8.
[94] D. Jia, W. Sun, D. Xu, L. Yu, X. Xin, W. Zhang, F. Qi, Abnormal dynamic recrystallization behavior of a nickel based superalloy during hot deformation, J. Alloy. Compd. 787 (2019) 196–205, https://doi.org/10.1016/j.jallcom.2019.02.055.
[95] J.N. DuPont, C.V. Robino, J.R. Michael, M.R. Nous, A.R. Marder, Solidification of Nb-bearing superalloys: Part I. Reaction sequences, Metall. Mater. Trans. A 29 (1998) 2785–2796, https://doi.org/10.1007/S11661-998-0319-3.
[96] J.N. Dupont, C.V. Robino, A.R. Marder, M.R. Notis, Solidification of Nb-bearing superalloys: part II. Pseudoternary solidification surfaces, Metall. Mater. Trans. A 29 (1998) 2797–2806, https://doi.org/10.1007/S11661-998-0320-X.
[97] D. Van, G.P. Dinda, J. Park, J. Mazumder, S.H. Lee, Enhancing hardness of Inconel 718 deposits using the aging effects of cold metal transfer-based additive manufacturing, Mater. Sci. Eng. A. 776 (2020), 139005, https://doi.org/10.1016/j.msea.2020.139005.
[98] S.A. Oh, R.E. Lim, J.W. Aroh, A.C. Chuang, B.J. Gould, J.V. Bernier, N. Parab, T. Sun, R.M. Suter, A.D. Rollett, Microscale observation via high-speed X-ray diffraction of alloy 718 during In Situ laser melting, JOM 73 (2021) 212–222, https://doi.org/10.1007/s11837-020-04481-1.
[99] Y. Gao, Y. Ding, J. Chen, J. Xu, Y. Ma, X. Wang, Effect of twin boundaries on the microstructure and mechanical properties of Inconel 625 alloy, Mater. Sci. Eng. A. 767 (2019), 138361, https://doi.org/10.1016/j.msea.2019.138361.
[100] J.P. Oliveira, T.M. Curado, Z. Zeng, J.G. Lopes, E. Rossinyol, J.M. Park, N. Schell, F.M. Braz Fernandes, H.S. Kim, Gas tungsten arc welding of as-rolled CrMnFeCoNi high entropy alloy, Mater. Des. 189 (2020), 108505, https://doi.org/10.1016/j.matdes.2020.108505.